PEG-fibrinogen Hydrogels for Three-dimensional Breast Cancer Cell Culture

Shantanu Pradhan, Iman Hassani, Wen J. Seeto, Elizabeth A. Lipke*

Department of Chemical Engineering, Auburn University, Auburn, AL, USA 36849

Emails: szp0023@auburn.edu (S.P.); izh0008@auburn.edu (I.H.); seetowj@auburn.edu (W.J.S.)

Keywords: cancer tissue engineering; tumor microenvironment; engineered tumor model; biomimetic; mechanical stiffness

*Corresponding author, Email: elipke@auburn.edu; Tel.: +1-334-844-2003

PEG-fibrinogen Hydrogel-based Breast Tumor Model

Abstract: Tissue-engineered three-dimensional (3D) cancer models employing biomimetic hydrogels as cellular scaffolds provide contextual *in vitro* recapitulation of the native tumor microenvironment, thereby improving their relevance for use in cancer research. This study reports the use of poly(ethylene glycol)-fibrinogen (PF) as a suitable biosynthetic hydrogel for the 3D culture of three breast cancer cell lines: MCF7, SK-BR-3 and MDA-MB-231. Modification of the matrix characteristics of PF hydrogels was achieved by addition of excess poly(ethylene glycol) diacrylate, which resulted in differences in Young's moduli, degradation behavior, release kinetics and ultrastructural variations in scaffold microarchitecture. Cancer cells were maintained in 3D culture with high viability within these hydrogels and resulted in cell-type dependent morphological changes over time. Cell proliferation and 3D morphology within the hydrogels were visualized through immunofluorescence staining. Finally, spatial heterogeneity of colony area within the hydrogels was quantified, with peripheral cells forming colonies of higher area compared to those in the interior regions. Overall, PF-based hydrogels facilitate 3D culture of breast cancer cells and investigation of cellular behavior in response to varying matrix characteristics. PF-based cancer models could be potentially used in future investigations of cancer biology and in anti-cancer drug-testing applications.

INTRODUCTION

The development of three-dimensional (3D) tissue-engineered cancer models employing the use of biomimetic polymers for cell encapsulation and culture is an important step towards *in vitro* modeling of the disease for investigations of tumorigenic mechanisms and drug-testing applications.[1-4] In traditional drug testing approaches, cancer cells cultured on two-dimensional (2D) substrates are used for testing efficacies of potential candidate drugs. However, due to inherent differences between 2D cultured cells and those in native tumor tissue, many compounds fail to meet desired levels of efficacy and safety in clinical studies.[5,6] In order to bridge this gap in correlation, bioengineered cancer models have been developed by culturing cancer cells within 3D biomimetic scaffolds that mimic key aspects of the native tumor microenvironment under *in vitro* conditions.[6-8] These scaffolds used for simulating native extracellular matrix (ECM) characteristics are usually obtained from natural (*e.g.* collagen, Matrigel, agarose)[3,4,9,10], synthetic (*e.g.* poly(ethylene glycol), poly(lactic-co-glycolic acid))[11-13] or hybrid (combination of natural and synthetic) sources.[14,15]

One of the components of the native tumor ECM is fibrinogen, which is known to be secreted and deposited by cancer cells.[16,17] Fibrinogen (Fb) is a hexameric, nodular protein with a molecular weight of approximately 340 kDa and consisting of two sets of α, β and γ chains, linked by disulfide bonds.[18] When fibrinogen is covalently conjugated with poly(ethylene glycol) diacrylate (PEGDA), it forms PEG-fibrinogen (PF) via Michael-type addition reaction between thiol groups on the cysteine sites in the fibrinogen molecule and the PEGDA polymeric chains.[19] PF can be photocrosslinked to form hydrogels in the presence of Eosin Y using visible light under physiological temperature and pH.[20] This capability renders it suitable for encapsulation and culture of a wide variety of cell types including smooth muscle cells (SMCs), induced

pluripotent stem cells (iPSCs), chondrocytes and others.[21-23] Specific modifications of the PF precursor (variation in PEGDA chain length, incorporation of Pluronic F127 micelles) have been shown to cause significant changes in the microarchitecture and overall bulk properties of the resulting hydrogel and subsequent changes in cellular morphology and function.[19,22,24] Hence, PF hydrogels can be suitably modulated at the macro-, micro- and nano-scales to investigate cellular responses to varying microenvironmental cues.

In recent studies, 3D breast cancer models have been developed using various biomimetic materials for the investigation of tumorigenic phenomena such as cellular migration, angiogenesis, and metastasis and for anti-cancer drug testing.[1,2,25-30] Generally, breast cancer can be classified into three distinct molecular subtypes: luminal subtype (estrogen receptor positive (ER+)/progesterone receptor positive (PR+)/human epidermal growth factor receptor negative (HER2-)), HER-2 subtype (ER-/ PR-/HER2+), and triple negative subtype (ER-/ PR-/HER2-). In some previous studies, comparative 3D *in vitro* models representative of these subtypes have been developed;[2,25,31-34] however, the synergistic role of matrix stiffness and physical properties in modulating the morphology and behavior of these multiple cellular subtypes needs to be investigated in more detail.

In this study, we present a comparative investigation of three cancer cell lines, representing the major breast cancer subtypes, cultured within PF-based hydrogels and examine their morphological and growth features in response to varying matrix characteristics. Hydrogel matrix characteristics were modulated by the addition of excess PEGDA, which resulted in differences in compressive moduli, ultrastructural features, degradation and diffusion kinetics and subsequent variations in cellular behavior of the encapsulated cell lines. Overall, these findings are useful for engineering tumor scaffolds and matrices *in vitro* and for comparative

analysis of cancer cell behavior in modulated 3D microenvironments. The PF-based tumor models could be further extended for the investigation of specific tumorigenic mechanisms (*e.g.* epithelial-mesenchymal transition, angiogenesis and metastasis) and for use in anti-cancer drug testing applications.

MATERIALS AND METHODS

All chemicals were obtained from Sigma-Aldrich, St. Louis, MO, unless mentioned otherwise.

Cell culture and maintenance

MCF7 (ER+/PR+/HER2-) breast cancer cells were kindly provided by Dr. Richard Bird, College of Veterinary Medicine, Auburn University. SK-BR-3 (ER-/PR-/HER2+) breast cancer cells were obtained from Dr. David Riese, Harrison School of Pharmacy, Auburn University. MDA-MB-231 (ER-/PR-/HER2-, metastatic) breast cancer cells were provided by Dr. Robert Arnold, Harrison School of Pharmacy, Auburn University. MCF7 and MDA-MB-231 cells were cultured in DMEM (GIBCO®, Life Technologies, Carlsbad, CA) supplemented with 10% fetal bovine serum (Atlanta Biologicals, Norcross, GA), 1% (v/v) non-essential amino acids (NEAA) (Lonza, Walkersville, MD), 1% (v/v) penicillin/streptomycin (GIBCO®), 1% (v/v) Glutamax (GIBCO®), and 1% (v/v) sodium pyruvate (GIBCO®). SK-BR-3 cells were maintained in McCoy's 5a Modified media (VWR, Radnor, PA) with 10% FBS and 1% (v/v) penicillin/streptomycin.

PEG-fibrinogen synthesis and characterization

PEGDA was prepared as described previously.[11] Briefly, poly(ethylene glycol) (Molecular weight: 10kDA) was reacted with acryloyl chloride (molar ratio of 1:4) in anhydrous

dichloromethane with triethylamine (molar ratio of 1:2) under argon overnight at 25°C. The PEGDA obtained from the reaction was purified by phase separation using 1.5 M K_2CO_3. The organic phase containing PEGDA was dried using anhydrous $MgSO_4$ to remove any residual aqueous phase and filtered. Finally, PEGDA was precipitated in cold diethyl ether, filtered, and vacuum-dried overnight. The degree of acrylation was characterized by ^1H NMR and the PEGDA powder was stored at -20°C.

Bovine fibrinogen was covalently coupled to PEGDA according to established protocols[19]. Briefly, fibrinogen was dissolved in an 8 M solution of urea in 10 mM PBS at a concentration of 7 mg/ml. Tris (2-carboxyethyl) phosphine hydrochloride (TCEP-HCl) was added at a molar ratio of 1.5:1 TCEP to fibrinogen cysteines to the above solution and the final pH was adjusted to 8.0. PEGDA was dissolved in the 8 M urea-PBS buffer at 280 mg/ml, centrifuged, and the clear PEGDA solution was slowly added to the fibrinogen solution. The reaction was allowed to proceed for 3 hours at 25°C in the dark. The solution was then diluted with an equal volume of urea-PBS buffer and precipitated by adding it into acetone (J.T. Baker, Center Valley, PA) at a volumetric ratio of 4:1 of acetone to product solution. The precipitate was separated from the acetone by centrifugation, weighed and re-dissolved in urea-PBS buffer at 2.2 ml of buffer/g of precipitate. The product was dialyzed against 1 L sterile PBS over 24 hours (with three changes of PBS) at 4°C in the dark. The final product was aliquoted into sterile centrifuge tubes and stored at -80°C.

To characterize the synthesized PF, the protein concentration and the net solid weight of the dry product were determined. Briefly, the protein content of the final PF solution was measured using a standard Pierce™ BCA Protein Assay Kit (Thermo-Scientific, Rockford, IL). In order to measure relative PEG content, PF solution was aliquoted in glass vials, lyophilized,

and the net weight of the dry solid was determined. The PEGylation efficiency was calculated according to the previously established formula[35] as given below in Equation (1).

$$\varepsilon_{PEGylation} = \frac{[PEG]}{[Fibrinogen]} \times \text{theoretical} \left\{ \frac{MW_{Fibrinogen}}{29 \times MW_{PEG}} \right\} \quad (1)$$

Hydrogel fabrication and cell encapsulation

Poly(dimethyl siloxane) (PDMS) molds were prefabricated for hydrogel formation by preparing a PDMS sheet of thickness 600 μm between two glass slides separated by spacers. Each sheet was then punched using a biopsy punch (diameter: 4 mm) to obtain circular shaped molds. The PDMS molds were attached tightly to the bottom of a 6-well plate to prevent leakage of cell-hydrogel precursor. Hydrogel precursor was prepared by mixing PF solution in PBS with 1.5% (v/v) triethanolamine (TEOA), 37 mM 1-vinyl-2-pyrrolidinone (NVP), and 0.1 mM Eosin Y in PBS as photoinitiator. A volume of 10 μL of the precursor was pipetted into the PDMS mold and crosslinked via visible light exposure (Light intensity: 203 mW/cm^2) for 2 minutes. After 2 minutes, the PDMS mold was peeled off from the well plate leaving behind disc-shaped photocrosslinked hydrogels (4 hydrogels per 6-well). The PF hydrogels were allowed to swell in PBS overnight prior to further analysis. In order to modulate hydrogel characteristics, additional PEGDA (250 mg/ml in PBS) was added to the PF precursor at a volumetric ratio of 96:4 (PF+1%P) or 92:8 (PF+2%P) prior to photocrosslinking. To encapsulate cells within these PF-based hydrogels, cells maintained in 2D flasks were trypsinized, counted, and resuspended in polymer precursor at 20×10^6 cells/ml prior to photocrosslinking. Post encapsulation, the freely-floating cell-laden tumor constructs were maintained in their respective culture media through the duration of study with media being replaced every 3 days (Figure 1).

Mechanical characterization

In order to assess the effect of additional PEGDA incorporation on the Young's moduli of PF-based hydrogel matrices, fabricated tumor constructs were subjected to parallel-plate compression testing under physiological conditions using a CellScale Microsquisher® system and associated SquisherJoy software. Briefly, MCF7 cells encapsulated within PF-based hydrogels at 20×10^6 cells/ml were maintained in 3D culture for 5 days prior to mechanical testing. These tumor constructs (4 mm in diameter and 600 μm in thickness) were then loaded onto the Microsquisher® platform and maintained at 37°C in PBS, preconditioned for compression testing and made to undergo cycles of compression and relaxation at a rate of 5 μm/s for a minimum of 15% strain. The force-displacement data obtained from the compression test were converted to stress-strain curves and the lower portion of the curve (5-15% strain) was used to obtain a linear regression line and estimate the Young's moduli of the tumor constructs. A minimum of 3 samples were measured for each condition.

Ultrastructural characterization

The ultrastructural features of acellular hydrogels and tumor constructs were visualized through scanning electron microscopy (SEM). Acellular hydrogels were washed in PBS, cryo-frozen in liquid nitrogen and lyophilized for 3 hours. Tumor constructs were first washed with PBS, fixed with 4% glutaraldehyde for one hour, and then post-fixated with 2% osmium tetroxide for one hour, all at 25°C. The fixed constructs were dehydrated gradually in increasing concentrations of ethanol (30%, 50%, 70%, 90% and 100%, 10 minutes for each concentration) and finally chemically dried using hexamethyl disilazane (HMDS, Electron Microscopy Sciences, Hatfield, PA) for 3 hours. Dried samples were mounted on carbon taped-aluminum stubs, sputter-coated

with gold (Pelco SC-6 sputter coater) and imaged using scanning electron microscope (JEOL JSM-7000F). SEM images of the acellular hydrogels were analyzed for pore size, pore density and porosity using ImageJ software (NIH, version 1.48q) in manner similar to that described in previous studies.[36,37] A minimum of 50 pores per condition were analyzed for pore size determination and 5 representative images per condition were analyzed for pore density and porosity quantification. Individual pores in the representative SEM images were outlined manually in the ImageJ software and their mean geometric diameters were reported as pore size. The number of pores in specific sections of the SEM images (2500 μm^2 area) were manually counted and extrapolated on a per mm^2 area basis. For porosity analysis, the SEM images were binarized with pores appearing black and 'non-pore' regions appearing white. The total area covered by the black regions (pore regions) was measured and the divided by the total area of the image field of view (bulk hydrogel area) to obtain the percentage porosity for the respective conditions.

Degradation behavior analysis

The effect of additional PEGDA incorporation on the degradation profile of PF hydrogels was assessed. Briefly, fabricated PF-based hydrogels were allowed to swell in PBS overnight to achieve an equilibrium swollen state. The PF-based hydrogels were placed in 96 well plates and incubated in collagenase type 2 (Worthington, LakeWood, NJ) solution in PBS (1 mg/ml, 305 U/mg) at 37°C. Fluorescence images of hydrogels (owing to background green fluorescence of Eosin Y photoinitiator) were captured at 15 minute intervals at a constant exposure time (150 ms) post incubation. These images were analyzed in ImageJ to assess changes in hydrogel area and fluorescence intensity of released Eosin Y in the collagenase solution. The edges of the

hydrogels were demarcated and the area of the bounding circle was calculated as hydrogel area. The fluorescence intensity of a constant region (0.5 mm^2) outside the hydrogel edge was assessed to quantify the relative release of Eosin Y into the surrounding solution. A minimum of 4 hydrogels per condition were tested for the degradation assay.

Release kinetics analysis

The ability of PF-based hydrogels to release entrapped biomolecules and the effect of additional PEGDA in the PF hydrogel matrix on the release kinetics were analyzed. Briefly, TRITC-dextran (molecular weight: 4.4 kDa) was mixed with the hydrogel precursor at 10 mg/ml prior to crosslinking. The crosslinked hydrogels were placed in 96 well plates and incubated in PBS at 37°C. Every 15 minutes, 50 µl of PBS buffer was collected and replaced with an equal volume of fresh PBS. The collected PBS containing released TRITC-dextran was analyzed through a plate reader (Excitation: 540/25 nm, Emission: 590/35 nm). Known concentrations of TRITC-dextran in PBS were used for the standard curve, and fresh PBS without TRITC-dextran was used as the blank. The cumulative mass release of TRITC-dextran was analyzed from the fluorescence intensities and used to calculate the diffusion coefficient of TRITC-dextran according to the formula[38] given below in Equation (2).

$$\frac{M_t}{M_\infty} = 1 - \frac{8}{\pi^2} \exp\left[\frac{-D\pi^2 t}{4\delta^2}\right] \qquad (2)$$

where M_t is the mass of released TRITC-dextran at time t, M_∞ is the equilibrium mass of TRITC-dextran, M_t / M_∞ is the fractional mass of TRITC-dextran released, D is the diffusion coefficient and 2δ is the hydrogel thickness. A minimum of 4 hydrogels per condition were analyzed for the release study.

Morphological analysis

Morphological features indicative of cancer cell growth and cell spreading were quantified via phase contrast microscopy and image analysis through 15 days in culture. Post-encapsulation of cancer cells, tumor constructs maintained in 3D culture were imaged using a Nikon Ti inverted microscope equipped with an Andor Luca S camera every 3 days. Z-stacks (200 μm thickness with individual slices spaced 5 μm apart) obtained above were analyzed using ImageJ software to determine colony area, diameter, circularity, and aspect ratio (for MCF7 and SK-BR-3 cells) and cellular area, diameter, circularity, aspect ratio, and elongation length (for MDA-MB-231 cells). Specifically, colony or cellular morphologies were quantified by focusing through individual planes in a sequential manner from top to bottom of the z-stacks. Since, individual planes contain both in-focus and out-of-focus regions of interest, quantification of morphological features was conducted at only those planes where edges and boundaries of cells or colonies appeared sharpest and most distinct. For MCF7 and SK-BR-3 cells, any cells or colonies extending beyond the hydrogel edge were not taken into consideration; only the colonies which were completely encapsulated within hydrogel constructs were quantified. Similarly, for MDA-MB-231 cells, only those completely encapsulated within the hydrogel constructs were used for morphological analysis. A minimum of 50 colonies (for MCF7 and SK-BR-3 cells) or cells (for MDA-MB-231 cells) from 3 independent tumor constructs were analyzed for each time point and each condition.

Viability assay

Viability of cells within the tumor models were observed and quantified via fluorescence microscopy and image analysis. Briefly, tumor constructs maintained in culture through 15 days

were washed with PBS and incubated in Live/Dead® cell viability stain (Invitrogen, Carlsbad, CA) for 30 minutes. Excess Live/Dead stain was washed with PBS and z-stack images of the samples were acquired under an inverted Nikon Ti microscope. The z-stacks (200 μm thickness with individual slices being 5 μm apart) were analyzed using ImageJ software by manually counting the cells in each slice of the z-stack. A minimum of 5 z-stack images from 3 independent tumor constructs were quantified for each time point and each condition.

Immunofluorescence staining and imaging

The 3D morphology and proliferation of cancer cells within tumor constructs were visualized by immunostaining and confocal fluorescence microscopy and quantified via digital image analysis. Briefly, tumor constructs maintained in 3D culture through 15 days were washed with PBS, fixed with 4% paraformaldehyde (Electron Microscopy Sciences) for 1 hour at 25°C, permeabilized with 0.5% Triton-X for thirty minutes followed by incubation with blocking buffer (2% bovine serum albumin and 5% FBS in PBS) overnight. On the following day, the constructs were incubated with primary antibody for Ki67 (human anti-rabbit, Abcam, 1:100 dilution) for 3 hours followed by incubation with secondary antibody for Ki67 (Alexa Fluor 488 goat anti-rabbit, Invitrogen, 1:200 dilution) and Alexa Fluor 568 Phalloidin (Invitrogen, 1:200 dilution) for 3 hours. Finally, the constructs were stained with Hoechst 33342 (1:200 dilution) for one hour and washed with PBS. Immunostained tumor constructs were mounted on coverslips and imaged using confocal microscopy (Nikon AI Confocal Scanning Laser Microscope) to obtain z-stacks of regions near the construct periphery. Fluorescence z-stacks were analyzed using ImageJ software by manually counting the number of cells in the field of view positive for Ki67

expression. A minimum of 5 z-stacks from 3 independent tumor constructs were analyzed for each condition.

Statistical analysis

All statistical analysis was performed using Minitab 17 Statistical Software (Minitab Inc.). After checking for normality of distribution, One-way ANOVA with Tukey's family error rate of 5% was used to evaluate statistical significance between multiple groups, assuming equal variance and equal sample size of compared groups. In case of unequal variance between groups, the Games-Howell post-hoc test was employed following the ANOVA analysis. Unless otherwise indicated, $p < 0.05$ was considered statistically significant.

RESULTS

Mechanical and microarchitectural analysis of PF-based hydrogels

A number of techniques were used to determine specific characteristics of the synthesized biomaterial. The degree of acrylation of PEGDA, measured via ^{1}H NMR spectroscopy, was determined to be 96.0%. The fibrinogen concentration and the dry weight of PEGDA in the synthesized PF solution obtained after dialysis were determined to be 16.6 mg/ml and 21.5 mg/ml, respectively. The PEGylation efficiency calculated according to Equation (1) was 74.0%. Addition of 1.0% and 2.0% PEGDA in the PF precursor resulted in protein concentration of 16.0 mg/ml and 15.3 mg/ml, respectively, and PEGDA concentration of 30.6 mg/ml and 39.8 mg/ml, respectively. The final composition of the three hydrogel formulations used were: PF: % Mass of total polymer = 3.8% w/v, Molar ratio of PEG: fibrinogen = 44:1; PF+1%P: % Mass = 4.7% w/v, Molar ratio = 65:1 and PF+2%P: % Mass = 5.5% w/v, Molar ratio = 88:1.

Mechanical characterization of tumor constructs was conducted 5 days post cell encapsulation in order to allow encapsulated cells to acclimatize within the 3D hydrogel microenvironment and attain their characteristic morphologies. The stress-strain curves for all three hydrogel compositions were linear and elastic in the 15% strain range (Fig. 2A). The Young's moduli for the three hydrogel compositions were evaluated as 3.2 ± 0.5 kPa (PF), 5.4 ± 0.5 kPa (PF+1%P) and 9.0 ± 1.4 kPa (PF+2%P), which were significantly different from each other (Fig. 2B). Thus, addition of excess PEGDA significantly increases the Young's moduli of cell-laden PF-based tumor constructs.

Acellular hydrogel constructs were visualized via SEM to observe stiffness-dependent ultrastructural variations. All three hydrogel compositions (PF, PF+1%P, PF+2%P) displayed a uniform, porous architecture with good pore interconnectivity (Fig. 2C-E). PF hydrogels exhibited a rougher surface with the presence of microgrooves and sub-micron pores, while PF+2%P hydrogels had a smoother and more structured appearance, indicating that the excess PEGDA promotes a firmer matrix with self-supporting microarchitectural features (Fig. 2F-H). Quantification of pore size of these PF-based hydrogels (based on 500X magnification images) revealed the average pore size of PF, PF+1%P and PF+2%P hydrogels to be 4±1 μm, 8±3 μm and 16±4 μm respectively, which were significantly different from each other (Fig. 2I). In addition, the pore density of PF hydrogels (50000 ± 4000 pores/mm^2) was significantly higher than that of PF+1%P hydrogels (39000 ± 5000 pores/mm^2) and PF+2%P hydrogels (20000 ± 5000 pores/mm^2) (Fig. 2J). Interestingly, the porosity of the three different hydrogel compositions (PF: 49 ± 3%, PF+1%P: 50 ± 5% and PF+2%P: 52 ± 2%) were comparable with each other (no significant difference), indicating that as the relative PEGDA concentration

increases, the pores become larger in size but less numerous, thereby maintaining relative consistency in the overall porosity of the PF-based hydrogels.

Ultrastructural visualization of tumor constructs revealed prominent cell line-dependent variations. MCF7 cells in PF hydrogels formed distinct colonies, particularly at the edges of the tumor constructs (Suppl. Fig. 1A and D), while cells in the middle regions appeared more isolated (Suppl. Fig. 1G). Closer inspection of the MCF7 cell surface revealed the presence of numerous microvilli and other cell-surface projections that are potentially involved in diverse cell-cell and cell-matrix interactions (Suppl. Fig. 1J and M).

SK-BR-3 cells also displayed a similar ultrastructural morphology in PF hydrogels. The cells formed local colonies, though these colonies were of smaller size compared to MCF7 cells (Suppl. Fig. 1B). As observed earlier with MCF7 cells, SK-BR-3 cells at the edge of tumor constructs formed larger colonies compared to those in the middle regions which appeared more isolated (Suppl. Fig. 1E and H). At higher magnification, the mesh-like nature of the matrix was visible and cell-surface projections of SK-BR-3 cells appeared vastly different from those of MCF7 cells (Suppl. Fig. 1K and N).

MDA-MB-231 cells appeared to be distributed as single cells within the hydrogel matrix without the presence of major cell-cell junctions (Suppl. Fig. 1C), as is characteristic of their metastatic nature. On closer inspection at the edges and middle regions of the tumor constructs, some cells appeared to be elongated or have cellular extensions while other appeared more rounded (Suppl. Fig. 1F and I). At higher magnifications, the mesh-like appearance of the hydrogel matrix and microvilli and filopodia at the cell surface interacting with the surrounding matrix were distinctly visible (Suppl. Fig. 1L and O), which were consistent with observations in a previous study with fibroblasts cultured in collagen scaffolds.[39]

Analysis of biodegradability of PF-based hydrogels

In order to assess the relative influence of additional PEGDA moieties on the biodegradability of PF-based hydrogels, enzymatic degradation of the hydrogels using collagenase II was conducted and degradation behavior over time was observed. Photocrosslinked PF-based hydrogels appeared green in color due to background fluorescence of Eosin Y photoinitiator (Fig. 3A, D, G). With the progress of degradation over time, the Eosin Y appeared to leach out into the surrounding solution as a result of hydrogel matrix disassembly (Fig. 3C, F, I). PF hydrogels displayed significant reduction in hydrogel area over time with no further trace of the hydrogel at the end of 180 minutes (Fig. 3A, B, C, J). However, PF+1%P and PF+2%P hydrogels did not exhibit any significant changes in area over 180 minutes or even after 3 days in incubation (Fig. 3D-I, J). PF hydrogels were also observed to undergo complete disassembly with increasing Eosin Y fluorescence in the surrounding collagenase solution over time (Fig. 3A-C, K). Though bulk disassembly of PF+1%P and PF+2%P hydrogels was not as prominent as PF hydrogels, Eosin Y within the hydrogels of PF+1%P and PF+2%P groups was also observed to leach out to a lesser extent, indicating that some degree of proteolytic degradation occurred within these hydrogels (Fig. 3K).

Release behavior of PF-based hydrogels

The influence of relative PEGDA concentration on the release behavior of entrapped TRITC-dextran from PF-based hydrogels was investigated. Based on fluorescence intensity of TRITC-dextran, PF hydrogels demonstrated the fastest and highest release of TRITC-dextran as compared to PF+1%P and PF+2%P hydrogels (Fig. 4A). The release kinetics was plotted

according to equation (2) (Fig. 4B) and the diffusion coefficients for the three hydrogel compositions were calculated based on Fick's law. The diffusion coefficient of PF hydrogels was calculated as $2.3\times10^{-11} \pm 1.6\times10^{-12}$ m^2/s which was significantly higher than that obtained for PF+1%P hydrogels ($7.5\times10^{-12} \pm 2.3\times10^{-12}$ m^2/s) and PF+2%P hydrogels ($4.6\times10^{-12} \pm 1.2\times10^{-12}$ m^2/s) (Fig. 4C). These observations indicate that the presence of additional PEGDA significantly reduces the ability of entrapped biomolecules to be released from the hydrogel matrix.

Cancer cell morphology within PF-based hydrogels

In order to assess the impact of modulated hydrogel characteristics on encapsulated cancer cells, PF-based tumor constructs were imaged via phase-contrast microscopy and images were analyzed for morphological features indicative of cancer cell growth and spreading. MCF7 cells encapsulated within tumor constructs appeared as individual cells on day 0 which progressed to form distinct locally distributed colonies through day 15 of culture, especially near hydrogel construct edges (Fig. 5A-D, Suppl. Video 1). Cells in PF+2%P hydrogels formed significantly larger colonies (based on colony area and diameter) compared to cells in PF hydrogels (Fig. 5E, F; Suppl Fig. 2A, B). However, colony circularity and colony aspect ratio (indicative of invasiveness) remained fairly comparable among the three groups (Fig. 5G, H; Suppl Fig. 2C, D).

SK-BR-3 cells also showed similar morphological characteristics with single cells on day 0 forming distinct cell colonies through day 15 (Fig. 6A-D, Suppl. Video 2). However, no significant difference was observed in colony area or diameter among the three hydrogel groups, suggesting that SK-BR-3 cells may be less responsive to changes in matrix characteristics

compared to MCF7 cells (Fig. 6E, F; Suppl. Fig. 3A, B). Notably, SK-BR-3 cells formed smaller colonies in the tumor constructs compared to MCF7 cells for all the three hydrogel compositions (~2000 μm^2 area for SK-BR-3 cells vs. ~3000 μm^2 for MCF7 cells). As reported above for MCF7 cells, colony circularity and aspect ratio remained fairly constant throughout the culture period (Fig. 6G, H; Suppl. Fig. 3C, D).

However, MDA-MB-231 cells, being metastatic in nature, formed cellular protrusions with gradual elongation of cells and apparent invasion of individual cells within the hydrogel matrix over time (Fig. 7A-D, Suppl. Video 3). Elongated cells were also observed to form cellular interconnections with each other via protrusions (Fig. 7B). Interestingly, a distinct proportion of MDA-MB-231 cells were observed to remain spherical in shape throughout the 15 day culture period, without committing to an invasive morphology (Fig. 7C, D; Suppl. Video 3). The percentage of cells exhibiting rounded morphology on day 15 were approximately 46%, 78% and 94% in the PF, PF+1%P and PF+2%P hydrogels respectively, differing significantly between hydrogel compositions. Cellular area and diameter remained fairly uniform over time; however, cells in the PF hydrogels displayed significantly higher cellular area and diameter (Fig. 7E, F; Suppl. Fig. 4A, B) compared to PF+1%P and PF+2%P hydrogels. Cellular circularity and aspect ratio (indicative of invasiveness) were also significantly different between hydrogels of the three different compositions (Fig. 7G, H). Average cellular elongation length was significantly higher in PF hydrogels (Suppl. Fig. 5, 6). These observations can be attributed to PF hydrogels potentially having higher biodegradability, higher bioactive ligand density, lower crosslinking density and higher degree of pore interconnectivity compared to PF+1%P and PF+2%P hydrogels, thereby allowing a higher number of cellular protrusions and greater degree of invasion. Notably, standard deviations of measured parameters were considerably higher for

MDA-MB-231 cells compared to the other two cell lines. This can be attributed to the presence of a distinct sub-population of cells that remained spherical in shape, potentially quiescent in behavior, without displaying any invasive morphology through the entire culture period.

Overall, morphological features of encapsulated cancer cells in PF-based hydrogels of varying composition were primarily cell-type dependent. Cells of epithelial phenotype (MCF7, SK-BR-3) displayed tight colony formation and local growth while cells of mesenchymal phenotype (MDA-MB-231) exhibited invasive morphologies. Additionally, variations in matrix compressive moduli and pore characteristics also influenced 3D morphology and behavior.

Cell viability within PF-based hydrogels

In order to assess the viability of the encapsulated cancer cells in 3D culture, the PF-based tumor constructs were stained with Live/Dead dye and cell viability was evaluated via fluorescence imaging. On day 0 immediately after encapsulation, all cell lines displayed high viability (>90%) irrespective of matrix stiffness. No significant effect of stiffness or trend was observed on viability for any cell line and viable cells appeared to be fairly well-distributed throughout the tumor constructs, with no obvious locational differences (Fig. 8A-L). Interestingly, MDA-MB-231 cells that appeared rounded in shape within PF-based hydrogels also demonstrated high viability, indicating that these cells were non-invasive and potentially quiescent in terms of proliferative and metabolic behavior (Fig. 8J, K, L). In some cases, at the final time point on day 15 of culture, there was a significant reduction in cell viability compared to day 0 values across the three cell lines and three matrix stiffnesses; however, these day 15 values still remained relatively high (>80%), indicating good viability of cells within tumor constructs over time (Fig. 8M).

Morphology and proliferation of cells in 3D culture

In order to characterize 3D morphology and quantify proliferation of cancer cell lines, the PF-based tumor constructs of varying stiffness were stained with phalloidin to visualize actin filaments and for Ki67 to identify proliferating cells and imaged under confocal microscopy. MCF7 cells were observed to form local, circular colonies with actin filaments localized at the periphery of cells. Approximately 70% of cells stained positively for Ki67 in hydrogels of varying stiffness, indicating relatively high cell proliferation irrespective of matrix stiffness (Fig. 9A-C, J).

SK-BR-3 cells also showed similar behavior within the tumor constructs. These cells also appeared as local colonies replicative of their native morphology with approximately 80% of the cells staining positive for Ki67 (Fig. 9D-F, J). No stiffness-dependent differences in cellular proliferation were observed in the SK-BR-3 tumor constructs.

MDA-MB-231 cells displayed an invasive morphology with cellular extensions within the 3D hydrogel matrix. Cells within PF hydrogels displayed highest degree of filopodial extensions and elongations, which was gradually reduced in hydrogels with increasing PEGDA concentration and increasing stiffness (Fig. 9G-I, J). Interestingly, a significant proportion of MDA-MB-231 cells remained circular in shape without displaying an invasive phenotype and this proportion gradually increased with increasing stiffness. In addition, cells with an invasive morphology exhibited nuclear Ki67 expression, while those with a rounded morphology exhibited cytoplasmic Ki67 expression. Cytoplasmic/membranous staining of Ki67 has been previously reported and has been correlated with high grade, ER- tumors with HER2 amplification.[40,41] Possible explanations for this observation include cross-reactivity with other

analogous proteins or relocalization of Ki67 within cells.[40] It could also be attributed to the presence of five different isoforms of the Ki67 protein (α, β, γ, δ and ε) which have been reported in literature; although their functional roles have not been investigated in detail.[42] It is possible to surmise that Ki67 positivity alone may not be sufficient to comprehensively describe the proliferation status of MDA-MB-231 cells and further investigation is necessary to distinguish truly proliferative cells from quiescent ones.

Locational growth heterogeneity in PF-based tumor constructs

Cancer cells found in native tumor tissue exhibit significant heterogeneity in growth characteristics, proliferation, metabolism, hypoxia and other cellular signaling mechanisms.[43,44] In this context, we observed locational growth heterogeneity in the tumor constructs, specifically with MCF7 and SK-BR-3 cells, via analysis of cell colony size on days 0, 7 and 15. When imaged on day 15, MCF7 and SK-BR-3 cells appeared to form large local colonies near the hydrogel edge, which gradually reduced in size towards the hydrogel interior (Fig. 10A-D). Analysis of colony area revealed that on day 0, MCF7 and SK-BR-3 cells appeared as single cells distributed uniformly throughout the tumor constructs. However on days 7 and 15, colony area of both cell types was distinctly higher near the hydrogel edge compared to that in the interior regions (Fig. 10 H, I, Suppl. Fig. 7). In comparison, no prominent location-dependent differences were observed in the morphology of MDA-MB-231 cells. Further investigation of cell proliferation revealed that in case of MCF7 and SK-BR-3 cells, more Ki67+ cells were localized near the tumor construct periphery and gradually decreased in number beyond a distance of ~ 500 μm from the hydrogel edge (Fig. 10E). Spatial variation in the density of Ki67+ cells and colony size correlated well, with higher numbers of proliferative cells and larger

colonies at the construct edge (indicative of extensive cell growth) and lower numbers of proliferative cells and smaller colonies in the interior regions of the construct (indicative of quiescent behavior) (Fig. 10E-G). However, no distinct effect of matrix composition on cellular heterogeneity was observed, with cells in hydrogels of varying composition exhibiting similar trends in colony area.

These observations could be attributed to the fact that cancer cells near the edge have better access to nutrients and oxygen from media diffusing near the edge of the hydrogel; however, as the diffusion distance increases, mass transfer resistance prevents cells in the interior regions from being proliferative or metabolically active. In addition, as the cell colonies near the edge become larger with time, the colonies themselves impart intrinsic resistance to the diffusion of nutrients to cells located in the interior regions of the hydrogels, further enhancing the locational differences in colony area.

DISCUSSION

The present study establishes a biomimetic *in vitro* model of three molecular subtypes of breast cancer and investigates the influence of matrix composition on the growth, morphology and spatial heterogeneity of encapsulated cells maintained in 3D culture. Establishing 3D biomimetic microenvironments in tissue-engineered cancer models is essential for recapitulating intrinsic tumorigenic characteristics of cancer cells including cellular mechanobiology, cell-cell and cell-matrix signaling. Towards this end, PEG-fibrinogen (PF) has been employed as a suitable biomaterial for establishing 3D tumor models. Though a number of natural and synthetic materials have been used for establishing 3D cancer models, the use of fibrinogen as a potential ECM scaffold for cancer cell studies has not been investigated in detail. The native breast tissue

ECM is mainly composed of fibrillar collagens, laminin, tenascin, fibronectin and other proteins.[45,46] In addition to these proteins, fibrinogen has been found to be an influential constituent of the ECM in normal and malignant breast stroma, promoting tumorigenic progression not only through integrin-mediated cancer cell-matrix interactions, but also by stimulating angiogenic growth via endothelial cell communications.[16,47-49] Hence, detailed investigation of the interactions between breast cancer cells and ECM fibrinogen is of potential interest in discovering novel therapeutic targets for drug treatment strategies.

In addition to cell-matrix signaling mechanisms, the bulk stiffness of the breast tissue (imparted by the cells and ECM matrix components) is also a driving factor in malignant behavior.[50,51] In an investigation of clinical breast tumor samples,[52] normal fat and fibroglandular tissue exhibited Young's moduli of ~3 kPa and fibroadenoma and low grade IDC (invasive ductal carcinoma) exhibited a moduli of 6-10 kPa. However, with evolution of tumor stage, the moduli increased to ~15-20 kPa for DCIS (ductal carcinoma in situ) and intermediate grade IDC, and ~ 40 kPa for high grade IDC.[52] Biomaterial-based *in vitro* tumor models also exhibit a wide range of stiffness values. Soft fibrin gels used for culturing B16-F1 melanoma cells demonstrated higher tumorigenicity in 100 Pa gels compared to 400 Pa or 1000 Pa gels (gel stiffness corresponding to initial measurements of cellular constructs).[53] Human head and neck squamous carcinoma cells cultured within alginate beads across a wide range of stiffnesses demonstrated higher enrichment of tumor initiating cells in moderate stiffness (70 kPa) hydrogels compared to soft (20 kPa) or hard (105 kPa) stiffness hydrogels (stiffness being measured in acellular constructs).[54] In comparison, acellular PF hydrogels have been shown to be relatively soft in terms of stiffness (~0.01-0.10 kPa), with the Young's moduli dependent on molecular weight of PEGDA crosslinkers (4-20 kDa) and the relative PEGDA content (10-20% w/v) in the polymer

precursor.[19] In previous studies, shear storage moduli (G') of acellular PF, PF+1%P and PF+2%P hydrogels were reported as ~120 Pa, ~350 Pa and ~700 Pa respectively [22] and the compressive moduli of acellular PF, PF+1%P and PF+2%P hydrogels were reported as 448 Pa, 1008 Pa and 2306 Pa respectively.[21]

Interestingly, incorporation of breast cancer cells within tumor constructs significantly increased the stiffness range to ~3-9 kPa, as compared to acellular PF hydrogels, indicating that the encapsulated cells themselves were a major contributor to the stiffness of PF-based tumor constructs, in addition to the hydrogel matrix per se. Although the Young's moduli of the tumor constructs were close to that of low-grade IDC, even moderate variations in matrix stiffness and microarchitectural properties elicited a prominent response in breast cancer cell behavior. The stiffness of PF-based tumor constructs is expected to further increase with time, as was demonstrated earlier with fibroblasts,[55] and potentially vary with the morphology and spreading behavior of encapsulated cancer cells. Reciprocally, the dynamic changes in stiffness could also affect cancer cell-matrix signaling mechanisms and induce genetic, proteomic and morphological changes at the cellular and tissue scales. When reporting stiffness of hydrogel constructs, it is important to consider the presence of encapsulated cells and their ability to dynamically modulate tissue characteristics over time. The cell density in native tumor tissue is of the order of 10^8 cells/ml.[56,57] Previously, we have encapsulated MCF7 cells within PEGDA tumor millibeads (2 mm in diameter) at 60×10^6 cells/ml and observed the formation of a central region of dead cells and a peripheral rim of viable cells, representative of the necrotic core of native tumors.[11] In our experience, high encapsulation densities and dense cell colonies at the hydrogel edge are necessary to establish a mass transfer gradient from the hydrogel periphery to the hydrogel

interior for constructs of these dimensions and thereby demonstrate locational tumor heterogeneity as described in Figure 10.

Besides bulk stiffness, other parameters including pore characteristics, degradability and diffusion kinetics could also play a synergistic role in determining cancer cell behavior in 3D microenvironments. Specifically, in this study, degradation and diffusion kinetics were found to vary significantly with the incorporation of additional PEGDA in the PF matrix. The proteolytic degradation of PF-based hydrogels is dependent in part on the diffusion of collagenase through the hydrogel matrix, as well as the relative accessibility of fibrinogen cleavage sites in the matrix to enzymatic activity. The degradation behavior of PF-based hydrogels indicates a reduction in enzymatic activity with increase in relative PEGDA content. In order to test whether the presence of additional PEGDA (and subsequent higher crosslinking density) hinders the accessibility of fibrinogen proteolytic sites to collagenase activity, the diffusion of collagenase in the PF-based hydrogel networks was modeled as shown earlier.[35] The effective diffusion coefficients of collagenase in PF-based hydrogels were estimated based on the degradation behavior in Fig. 3K and using Equation (2):

$$\frac{M_t}{M_\infty} = 1 - \frac{8}{\pi^2} \exp\left[\frac{-D\pi^2 t}{4\delta^2}\right] \qquad (2)$$

where now M_t is the mass of the degraded hydrogel at time t, M_∞ is the mass of hydrogel degraded at the equilibrium state, M_t / M_∞ is the fractional mass of the degraded hydrogel, D is the effective diffusion coefficient and 2δ is the thickness of the hydrogel, with the assumption that the rate of Eosin Y released is proportional to the rate of mass loss of the degraded hydrogel. The estimated effective diffusion coefficients of collagenase in PF, PF+1%P and PF+2%P hydrogels were calculated as $12.0\times10^{-12} \pm 1.8\times10^{-12}$ m^2/s, $9.6\times10^{-12} \pm 0.8\times10^{-12}$ m^2/s and $8.0\times10^{-12} \pm 1.3\times10^{-12}$ m^2/s respectively (Suppl. Fig. 8). These data indicate that collagenase diffusion

within PF-based hydrogels decreases with increasing PEGDA concentration and subsequent structural alterations in the hydrogel assembly. Thus the degradation kinetics of PF-based hydrogels is partly mediated by the relative accessibility of fibrinolytic cleavage sites within the hydrogel matrix which is blocked by the presence of additional PEGDA moieties. However, at high collagenase concentrations, the rate of hydrogel disassembly and proteolytic degradation is expected to be greater than the rate of collagenase diffusion through the hydrogel network.

Matrix stiffness and porosity are important factors affecting the cellular fate of encapsulated cancer cells within engineered tissue constructs.[46,58] In this study, the stiffness and pore characteristics of PF-based hydrogels were coupled with each other, which is a limitation of this hydrogel platform. Addition of excess PEGDA resulted in increasing stiffness while at the same time, increasing pore size and decreasing pore density. Further assessment of pore size of hydrogel matrices revealed an interesting trend in observations. The hindered solute diffusion in solvent-filled pores model was used to estimate the effective pore size of PF-based hydrogel matrices using the following equation as described earlier.[59]

$$\frac{D}{D_0} = (1 - \lambda^2)\,(1 - 2.1044\lambda + 2.089\lambda^3 - 0.948\lambda^5) \qquad (3)$$

Where D is the diffusion coefficient of TRITC-dextran within PF-based hydrogels, D_0 is the diffusion coefficient of TRITC-dextran calculated from the Stokes-Einstein's equation (14.6×10^{-11} m^2/s) and λ is a characteristic ratio of TRITC-dextran hydrodynamic diameter to average pore diameter of hydrogel matrix.

The effective theoretical pore diameter obtained from the above model for the PF, PF+1%P and PF+2%P hydrogels were calculated as 6.4±3.3 nm, 4.5±3.5 nm and 3.9±3.3 nm respectively. These pore sizes are significantly smaller than those estimated via SEM image quantification and indicate decreasing pore size with increasing relative PEGDA concentration. The theoretical pore

size estimates correlate well with the observed diffusional behavior of TRITC-dextran and collagenase. One possible explanation for the disparity in the theoretical and experimental measurements lies in the methodology and limitations of the estimation techniques. SEM imaging allows for the visualization of larger macromolecular structures and surface features that may not be accounted for in theoretical models; quantification of SEM images tends to bias the results towards larger micron-scale features rather than nano-scale features. On the other hand, theoretical models may not fully encompass the entirety of the physical characteristics presented by the hydrogel matrices due to limitations of model assumptions and may be biased towards nano-scale pore size estimates. Specifically, this model assumes the hydrogel pores as close-packed cylinders of uniform diameter and of size comparable to solute hydrodynamic radius. Pore size estimates obtained from SEM images are hindered by the dehydration and possible shrinkage of the hydrogel sample during preparation. SEM images provide an incomplete view of the porous network of the hydrogel matrices and pore size quantification is only limited to specific planes and orientations of view of the hydrogel surface. Also, the porosity values estimated for the hydrogel matrices only account for the macro-scale porous structures rather than the nano-scale pores within the matrices which cannot be visualized via SEM. Hence, both techniques, theoretical model estimation and experimental SEM quantification are necessary to obtain a complete picture of the pore size characteristics of PF-based hydrogels.

Future investigations of material design and fabrication would focus on uncoupling the mutual dependence of individual parameters and study the resulting effects on 3D cell behavior. In a previous study, interpenetrating networks of reconstituted basement membrane matrix and alginate has been used to independently modulate matrix stiffness, composition and ligand

availability for the culture of normal mammary epithelial cells.[60] In addition, the responsiveness of encapsulated cells to independently modulated matrix stiffness, ECM chemistry and ligand density has also been investigated.[12,61] Application of these material design techniques to PF-based hydrogels could potentially provide additional information about cancer cell behavior in 3D microenvironments.

PF-based tumor models could also incorporate additional elements of the complex tumor microenvironment including cancer-associated fibroblasts, endothelial cells and macrophages. These models could be potentially used to assess the efficacy of anti-cancer drug compounds *in vitro* prior to *in vivo* testing, thereby obtaining more contextually relevant data compared to that obtained through traditional 2D culture systems. The PF-based tumor model also offers an advantage over other traditional 3D tumor models through the ability to recapitulate the heterogeneity that is inherent to native tumors. Cells located at the native tumor periphery are in close proximity to neo-vasculature and hence richly supplied with nutrients and oxygen. However, cells located in the interior regions of the tumor tissue experience diffusional gradients of oxygen (leading to hypoxia) and nutrients (leading to accumulation of waste metabolites and acidic pH).[44,62] Previously, we have shown that MCF7 cells cultured within spheroidal PEGDA hydrogel millibeads (2 mm diameter) exhibit viable cell layers in the hydrogel periphery, but undergo significant cell death in the interior regions of the millibeads.[11] In another study, cancer cells encapsulated within transglutaminase-crosslinked gelatin hydrogels also displayed growth and morphological heterogeneity due to onset of hypoxia in the central regions of millimeter-scale large hydrogel constructs.[63] Since a distinct sub-population of MCF7, SK-BR-3 and MDA-MB-231 cells in the PF-based tumor constructs appear to be either non-proliferative or

morphologically non-invasive, these cells could be used in future investigations of tumor dormancy or cancer stem cell-like characteristics.

Overall, the use of PF-based hydrogels for 3D cancer cell culture presents a number of opportunities in the investigation of cancer mechanobiology and the role of the tumor microenvironment in malignant disease progression. Continued adaptation and optimization of this 3D culture platform could potentially facilitate wide spread applications in cancer cell studies and drug-testing platforms.

CONCLUSIONS

In this study, we have developed PEG-fibrinogen (PF) hydrogel-based tumor models for the 3D culture of breast cancer cell lines. Incorporation of additional PEGDA in the PF matrix led to an increase in Young's moduli, ultrastructural variations in hydrogel matrix and significant differences in biodegradability and diffusion kinetics of the hydrogels. Cancer cells were cultured within these hydrogels with high viability and exhibited cell type-dependent and stiffness-dependent variation in morphology, cell spreading and growth. 3D morphology was visualized and proliferation was quantified within the PF-based tumor constructs. Additionally, locational variation of colony size, indicative of tumor heterogeneity, was quantified within the tumor constructs. These tumor constructs can be used in the future for designing improved biomimetic models replicative of the native breast tumor microenvironment, further investigation of tumorigenic mechanisms and for use in anti-cancer drug-testing applications.

ACKNOWLEDGMENTS

The authors acknowledge financial support from the Auburn University Research Initiative in Cancer (AURIC) Graduate Fellowship program (S.P.), NSF (NSF-CBET-1150854) and NIH (SBIR Phase I grant, HHSN261201400037C). The authors are also grateful to the research group of Dr. C. Ross Ethier, Wallace H. Coulter Department of Biomedical Engineering, Georgia Institute of Technology, Atlanta, GA, USA for facilitating the use of the Microsquisher® system for mechanical characterization.

AUTHOR CONTRIBUTIONS

S.P. and E.A.L. conceived the project and designed the experiments. S.P. conducted the experiments and wrote the paper. I.H. assisted in cell culture, fluorescence imaging, and image analysis. W.J.S. assisted in SEM imaging and mechanical characterization. E.A.L. directed and oversaw the study. All authors provided input in the final preparation of the paper.

CONFLICT OF INTERESTS

The authors declare no conflict of interests.

REFERENCES

1. Estrada MF, Rebelo SP, Davies EJ, Pinto MT, Pereira H, Santo VE, Smalley MJ, Barry ST, Gualda EJ, Alves PM and others. Modelling the tumour microenvironment in long-term microencapsulated 3D co-cultures recapitulates phenotypic features of disease progression. Biomaterials 2016;78:50-61.
2. Bray LJ, Binner M, Holzheu A, Friedrichs J, Freudenberg U, Hutmacher DW, Werner C. Multi-parametric hydrogels support 3D in vitro bioengineered microenvironment models of tumour angiogenesis. Biomaterials 2015;53:609-20.
3. Chen L, Xiao Z, Meng Y, Zhao Y, Han J, Su G, Chen B, Dai J. The enhancement of cancer stem cell properties of MCF-7 cells in 3D collagen scaffolds for modeling of cancer and anti-cancer drugs. Biomaterials 2012;33(5):1437-44.

4. Szot CS, Buchanan CF, Freeman JW, Rylander MN. 3D *in vitro* bioengineered tumors based on collagen I hydrogels. Biomaterials 2011;32(31):7905-7912.
5. de Bono JS, Ashworth A. Translating cancer research into targeted therapeutics. Nature 2010;467(7315):543-549.
6. Cox MC, Reese LM, Bickford LR, Verbridge SS. Toward the broad adoption of 3D tumor models in the cancer drug pipeline. ACS Biomater. Sci. Eng. 2015;1(10):877-894.
7. Gu L, Mooney DJ. Biomaterials and emerging anticancer therapeutics: engineering the microenvironment. Nat Rev Cancer 2015;16(1):56-66.
8. Carvalho MR, Lima D, Reis RL, Correlo VM, Oliveira JM. Evaluating biomaterial- and microfluidic-based 3D tumor models. Trends Biotechnol 2015;33(11):667-78.
9. Vantangoli MM, Madnick SJ, Huse SM, Weston P, Boekelheide K. MCF-7 human breast cancer cells form differentiated microtissues in scaffold-free hydrogels. PLoS One 2015;10(8):e0135426.
10. Krause S, Maffini MV, Soto AM, Sonnenschein C. The microenvironment determines the breast cancer cells' phenotype: organization of MCF7 cells in 3D cultures. BMC Cancer 2010;10:263.
11. Pradhan S, Chaudhury CS, Lipke EA. Dual-phase, surface tension-based fabrication method for generation of tumor millibeads. Langmuir 2014;30(13):3817-3825.
12. Gill BJ, Gibbons DL, Roudsari LC, Saik JE, Rizvi ZH, Roybal JD, Kurie JM, West JL. A synthetic matrix with independently tunable biochemistry and mechanical properties to study epithelial morphogenesis and EMT in a lung adenocarcinoma model. Cancer Res. 2012;72(22):6013-6023.
13. Yang X, Sarvestani SK, Moeinzadeh S, He X, Jabbari E. Three-dimensional-engineered matrix to study cancer stem cells and tumorsphere formation: effect of matrix modulus. Tissue Eng. Part A 2013;19(5-6):669-84.
14. Fischbach C, Kong HJ, Hsiong SX, Evangelista MB, Yuen W, Mooney DJ. Cancer cell angiogenic capability is regulated by 3D culture and integrin engagement. Proc. Natl. Acad. Sci. USA 2009;106(2):399-404.
15. Kievit FM, Florczyk SJ, Leung MC, Veiseh O, Park JO, Disis ML, Zhang M. Chitosan-alginate 3D scaffolds as a mimic of the glioma tumor microenvironment. Biomaterials 2010;31(22):5903-10.
16. Simpson-Haidaris PJ, Rybarczyk B. Tumors and fibrinogen. The role of fibrinogen as an extracellular matrix protein. Ann. N. Y. Acad. Sci. 2001;936:406-25.
17. Rybarczyk BJ, Simpson-Haidaris PJ. Fibrinogen assembly, secretion, and deposition into extracellular matrix by MCF-7 human breast carcinoma cells. Cancer Res. 2000;60(7):2033-2039.
18. Hall CE, Slayter HS. The fibrinogen molecule: its size, shape, and mode of polymerization. J. Biophys. Biochem. Cytol. 1959;5(1):11-6.
19. Almany L, Seliktar D. Biosynthetic hydrogel scaffolds made from fibrinogen and polyethylene glycol for 3D cell cultures. Biomaterials 2005;26(15):2467-77.
20. Kerscher P, Turnbull IC, Hodge AJ, Kim J, Seliktar D, Easley CJ, Costa KD, Lipke EA. Direct hydrogel encapsulation of pluripotent stem cells enables ontomimetic differentiation and growth of engineered human heart tissues. Biomaterials 2016;83:383-95.

1. Peyton SR, Kim PD, Ghajar CM, Seliktar D, Putnam AJ. The effects of matrix stiffness and RhoA on the phenotypic plasticity of smooth muscle cells in a 3-D biosynthetic hydrogel system. Biomaterials 2008;29(17):2597-607.
2. Bearzi C, Gargioli C, Baci D, Fortunato O, Shapira-Schweitzer K, Kossover O, Latronico MV, Seliktar D, Condorelli G, Rizzi R. PlGF-MMP9-engineered iPS cells supported on a PEG-fibrinogen hydrogel scaffold possess an enhanced capacity to repair damaged myocardium. Cell Death Dis. 2014;5:e1053.
3. Appelman TP, Mizrahi J, Elisseeff JH, Seliktar D. The influence of biological motifs and dynamic mechanical stimulation in hydrogel scaffold systems on the phenotype of chondrocytes. Biomaterials 2011;32(6):1508-16.
4. Frisman I, Seliktar D, Bianco-Peled H. Nanostructuring biosynthetic hydrogels for tissue engineering: a cellular and structural analysis. Acta Biomater. 2012;8(1):51-60.
5. Peela N, Sam FS, Christenson W, Truong D, Watson AW, Mouneimne G, Ros R, Nikkhah M. A three dimensional micropatterned tumor model for breast cancer cell migration studies. Biomaterials 2016;81:72-83.
6. Seib FP, Berry JE, Shiozawa Y, Taichman RS, Kaplan DL. Tissue engineering a surrogate niche for metastatic cancer cells. Biomaterials 2015;51:313-9.
7. Zhu W, Wang M, Fu Y, Castro NJ, Fu SW, Zhang LG. Engineering a biomimetic three-dimensional nanostructured bone model for breast cancer bone metastasis study. Acta Biomater 2015;14:164-74.
8. Subia B, Dey T, Sharma S, Kundu SC. Target specific delivery of anticancer drug in silk fibroin based 3D distribution model of bone-breast cancer cells. ACS Appl Mater Interfaces 2015;7(4):2269-2279.
9. Rijal G, Li W. 3D scaffolds in breast cancer research. Biomaterials 2016;81:135-56.
0. Pradhan S, Hassani I, Clary JM, Lipke EA. Polymeric biomaterials for in vitro cancer tissue engineering and drug testing applications. Tissue Eng. Part B 2016.
1. Kenny PA, Lee GY, Myers CA, Neve RM, Semeiks JR, Spellman PT, Lorenz K, Lee EH, Barcellos-Hoff MH, Petersen OW and others. The morphologies of breast cancer cell lines in three-dimensional assays correlate with their profiles of gene expression. Mol. Oncol. 2007;1(1):84-96.
2. Ivascu A, Kubbies M. Diversity of cell-mediated adhesions in breast cancer spheroids. Int. J. Oncol. 2007;31(6):1403-13.
3. Feng S, Duan X, Lo PK, Liu S, Liu X, Chen H, Wang Q. Expansion of breast cancer stem cells with fibrous scaffolds. Integr. Biol. (Camb) 2013;5(5):768-77.
4. Hakanson M, Kobel S, Lutolf MP, Textor M, Cukierman E, Charnley M. Controlled breast cancer microarrays for the deconvolution of cellular multilayering and density effects upon drug responses. PLoS One 2012;7(6):e40141.
5. Dikovsky D, Bianco-Peled H, Seliktar D. The effect of structural alterations of PEG-fibrinogen hydrogel scaffolds on 3-D cellular morphology and cellular migration. Biomaterials 2006;27(8):1496-506.
6. Sokic S, Christenson M, Larson J, Papavasiliou G. In Situ Generation of Cell-Laden Porous MMP-Sensitive PEGDA Hydrogels by Gelatin Leaching. Macromol. Biosci. 2014;14(5):731-739.
7. Chiu YC, Larson JC, Isom A, Jr., Brey EM. Generation of porous poly(ethylene glycol) hydrogels by salt leaching. Tissue Eng. Part C 2010;16(5):905-12.
8. Karimi M. Diffusion in Polymer Solids and Solutions: Intech; 2011. 17-40 p.

9. Masci VL, Taddei AR, Gambellini G, Giorgi F, Fausto AM. Ultrastructural investigation on fibroblast interaction with collagen scaffold. J. Biomed. Mater. Res. A 2016;104(1):272-82.
0. Faratian D, Munro A, Twelves C, Bartlett JM. Membranous and cytoplasmic staining of Ki67 is associated with HER2 and ER status in invasive breast carcinoma. Histopathology 2009;54(2):254-7.
1. Grzanka A, Sujkowska R, Janiak A, Adamska M. Immunogold labelling of PCNA and Ki-67 antigen at the ultrastructural level in laryngeal squamous cell carcinoma and its correlation with lymph node metastasis and histological grade. Acta Histochemica 2000;102(2):139-149.
2. Schmidt MH, Broll R, Bruch HP, Finniss S, Bogler O, Duchrow M. Proliferation marker pKi-67 occurs in different isoforms with various cellular effects. J. Cell Biochem. 2004;91(6):1280-92.
3. Hirschhaeuser F, Menne H, Dittfeld C, West J, Mueller-Klieser W, Kunz-Schughart LA. Multicellular tumor spheroids: an underestimated tool is catching up again. J. Biotechnol. 2010;148(1):3-15.
4. Zhou J, Schmid T, Schnitzer S, Brüne B. Tumor hypoxia and cancer progression. Cancer Letters 2006;237(1):10-21.
5. Oskarsson T. Extracellular matrix components in breast cancer progression and metastasis. Breast 2013;22 Suppl 2:S66-72.
6. Lu P, Weaver VM, Werb Z. The extracellular matrix: a dynamic niche in cancer progression. J. Cell Biol. 2012;196(4):395-406.
7. Costantini V, Zacharski LR, Memoli VA, Kisiel W, Kudryk BJ, Rousseau SM. Fibrinogen deposition without thrombin generation in primary human breast-cancer tissue. Cancer Research 1991;51(1):349-353.
8. Kolodziejczyk J, Ponczek MB. The role of fibrinogen, fibrin and fibrin(ogen) degradation products (FDPs) in tumor progression. Contemp. Oncol. (Pozn) 2013;17(2):113-9.
9. Palumbo JS, Degen JL. Fibrinogen and tumor cell metastasis. Haemostasis 2001;31 Suppl 1:11-5.
0. Fenner J, Stacer AC, Winterroth F, Johnson TD, Luker KE, Luker GD. Macroscopic stiffness of breast tumors predicts metastasis. Sci. Rep. 2014;4:5512.
1. Butcher DT, Alliston T, Weaver VM. A tense situation: forcing tumour progression. Nat. Rev. Cancer 2009;9(2):108-22.
2. Samani A, Zubovits J, Plewes D. Elastic moduli of normal and pathological human breast tissues: an inversion-technique-based investigation of 169 samples. Phys. Med. Biol. 2007;52(6):1565-76.
3. Liu J, Tan Y, Zhang H, Zhang Y, Xu P, Chen J, Poh YC, Tang K, Wang N, Huang B. Soft fibrin gels promote selection and growth of tumorigenic cells. Nat. Mater. 2012;11(8):734-41.
4. Liu C, Liu Y, Xu XX, Wu H, Xie HG, Chen L, Lu T, Yang L, Guo X, Sun GW and others. Potential effect of matrix stiffness on the enrichment of tumor initiating cells under three-dimensional culture conditions. Exp. Cell. Res. 2015;330(1):123-34.
5. Kesselman D, Kossover O, Mironi-Harpaz I, Seliktar D. Time-dependent cellular morphogenesis and matrix stiffening in proteolytically responsive hydrogels. Acta Biomater. 2013;9(8):7630-9.

6. Stephens TC, Peacock JH. Cell yield and cell survival following chemotherapy of the B16 melanoma. Br. J. Cancer 1978;38(5):591-8.
7. Grantab R, Sivananthan S, Tannock IF. The penetration of anticancer drugs through tumor tissue as a function of cellular adhesion and packing density of tumor cells. Cancer Res. 2006;66(2):1033-9.
8. Levental KR, Yu H, Kass L, Lakins JN, Egeblad M, Erler JT, Fong SF, Csiszar K, Giaccia A, Weninger W and others. Matrix crosslinking forces tumor progression by enhancing integrin signaling. Cell 2009;139(5):891-906.
9. Cu Y, Saltzman WM. Mathematical modeling of molecular diffusion through mucus. Adv. Drug Deliv. Rev. 2009;61(2):101-114.
0. Chaudhuri O, Koshy ST, Branco da Cunha C, Shin JW, Verbeke CS, Allison KH, Mooney DJ. Extracellular matrix stiffness and composition jointly regulate the induction of malignant phenotypes in mammary epithelium. Nature Materials 2014;13(10):970-978.
1. Peyton SR, Raub CB, Keschrumrus VP, Putnam AJ. The use of poly(ethylene glycol) hydrogels to investigate the impact of ECM chemistry and mechanics on smooth muscle cells. Biomaterials 2006;27(28):4881-93.
2. Höckel M, Vaupel P. Tumor Hypoxia: Definitions and Current Clinical, Biologic, and Molecular Aspects. J. Ntl. Cancer Inst. 2001;93(4):266-276.
3. Fang JY, Tan SJ, Yang Z, Tayag C, Han B. Tumor bioengineering using a transglutaminase crosslinked hydrogel. PLoS One 2014;9(8):e105616.

FIGURE CAPTIONS

Figure 1. Schematic of hydrogel preparation and cell encapsulation. (A) PEG-fibrinogen (PF) is coupled with additional PEGDA (1% or 2% w/v) to form hydrogel matrices (PF+1%P or PF+2%P) with modified physical characteristics. (B) PDMS molds are used to form photocrosslinked cell-laden hydrogel constructs via visible light and maintained in 3D culture.

Figure 2. Mechanical and ultrastructural features of PF-based hydrogels. (A) Stress-strain relationship of PF-based tumor constructs demonstrates the influence of additional PEGDA moieties on the compressive behavior of hydrogels. (B) Incorporation of excess PEGDA results in increasing Young's modulus of tumor constructs (n=3 hydrogels, *$p<0.05$). (C-H) Representative SEM images of acellular hydrogels of different compositions (Top panel: 500X magnification; Bottom panel: 1000X magnification). (C and F) PF hydrogels exhibit a greater degree of surface roughness due to the presence of microgrooves and sub-micron pores and a higher degree of pore interconnectivity. (D and G) PF+1%P hydrogels reveal an increasing degree of groove-like features. (E and H) PF+2%P hydrogels display a smoother pore surface and a greater degree of self-supporting features. (I) Increase in pore size and (J) decrease in pore density with additional PEGDA incorporation in PF-based hydrogel matrices. Circles denote individual pore measurements, diamonds denote means of respective groups and rectangular boxes represent the lower quartile, median and upper quartile of respective groups (Pore size: n=50 pores, Pore density: n=5 representative regions of interest, *$p<0.05$).

Figure 3. Degradation behavior of PF-based hydrogels. (A-C) PF hydrogels undergo complete disassembly with leaching of Eosin Y over 180 minutes. (D-E) PF+1%P hydrogels and (G-I)

PF+2%P hydrogels remain intact in bulk structure over time. White line denotes the hydrogel edge and red line denotes the edge of the well. (J) PF hydrogels show significant reduction in hydrogel area compared to PF+1%P and PF+2%P hydrogels. (K) PF hydrogels undergo higher degree of Eosin Y release compared to PF+1%P and PF+2%P hydrogels (n=4 hydrogels, *$p<0.05$). Scale bar = 1 mm.

Figure 4. Release profile kinetics of PF-based hydrogels. (A) Percentage cumulative release profiles of entrapped TRITC-dextran from PF-based hydrogels demonstrate slower release rates with increasing PEGDA concentration. (B) Plot of $\ln(1-M_t/M_\infty)$ versus time for PF-based hydrogels. Correlation coefficients of fitted linear trendlines are presented adjacent to the respective trendlines. (C) Diffusion coefficients of TRITC-dextran released from PF-based hydrogels demonstrate significantly reduced values with the incorporation of additional PEGDA (n=4 hydrogels, *$p<0.05$).

Figure 5. MCF7 colony morphology over time. (A-D) Representative phase contrast images of MCF7 cells demonstrate local colony formation within PF-based hydrogels over 15 days in culture. (E) Increase in average colony area and (F) average colony diameter of MCF7 cells with time, with PF+2%P hydrogels displaying larger colony formation. (G) Average colony circularity and (H) average colony aspect ratio remain fairly constant among the three groups (Data presented as average of 3 independent tumor constructs, n = 50 colonies, * significant difference between PF and PF+2%P, # significant difference between PF and PF+1%P, $p<0.05$). Scale bar = 50 μm.

Figure 6. SK-BR-3 colony morphology over time. (A-D) Representative phase contrast images of SK-BR-3 cells demonstrate local colony formation within PF-based hydrogels over 15 days in culture. (E) Increase in average colony area and (F) average colony diameter of SK-BR-3 cells with time. (G) Average colony circularity and (H) average colony aspect ratio remain fairly constant with time (Data presented as average of 3 independent tumor constructs, n = 50 colonies, no significant difference between three groups, $p<0.05$). Scale bar = 50 μm.

Figure 7. MDA-MB-231 cell morphology over time. (A-D) Representative phase contrast images of MDA-MB-231 cells exhibit invasive and elongated morphologies within PF-based hydrogels while some cells remain spherical in shape and non-committed towards an invasive morphology. (E) Cellular area and (F) cellular diameter of MDA-MB-231 cells remain fairly uniform over time, with PF hydrogels displaying higher cellular size. (G) Cellular circularity and (H) cellular aspect ratio are also significantly different between hydrogels of three different compositions (Data presented as average of 3 independent tumor constructs, n = 50 cells, * significant difference between PF and PF+2%P, # significant difference between PF and PF+1%P, $p<0.05$). Scale bar = 50 μm.

Figure 8. Cell viability in PF-based hydrogels. (A-L) Representative fluorescence z-stacks (thickness = 200 μm) of cells within PF-based tumor constructs stained with calcein AM (Live, green) and ethidium homodimer (Dead, red) on days 0 and 15 demonstrate uniform distribution of live cells. (M) MCF7, SK-BR-3 and MDA-MB-231 cells exhibit relatively high cell viability through 15 days of culture, irrespective of matrix stiffness, thereby demonstrating that matrix stiffness does not influence cell viability; temporal changes in viability were observed in some

conditions (n = 5 z-stacks from at least 3 independent tumor constructs, *p<0.05). Scale bar = 100 μm.

Figure 9. Cell line- and stiffness-dependent morphology and proliferation within PF-based hydrogels. (A-I) Representative fluorescence images of cells within tumor constructs on day 15 post-encapsulation. Scale bar = 100 μm. (Inset - magnified view of corresponding image, Scale bar: 50 μm). (A-C) MCF7 and (D-F) SK-BR-3 cells display local colony formation with cells stained for actin filaments (red, cell morphology), Ki67 (green, cell proliferation), and nuclei (blue). (G-I) MDA-MB-231 cells display elongated morphology in PF hydrogels which decreases with increasing PEGDA content. (J) Relative percentage of Ki67 positive cells for cancer cell lines in PF-based hydrogels (n= 5 z-stacks from at least 3 independent tumor constructs).

Figure 10. Locational heterogeneity in tumor constructs. Representative phase contrast images of (A) MCF7 cells cultured within PF hydrogels and imaged on day 15 exhibit locational differences in colony size with (B) those near the edge appearing largest in size, (C) those in the intermediate zone appearing smaller, and (D) those in the innermost zone appearing isolated and smallest in area. (E, F, G) Representative fluorescence images of MCF7 cells positive for Ki67 (proliferative cells) are located closer to the hydrogel edge while those in the hydrogel center appear non-proliferative and quiescent. White dotted lines represent hydrogel edge. Analysis of phase contrast images of (H) MCF7 and (I) SK-BR-3 cells reveal that cells are uniformly sized throughout hydrogel constructs on day 0, but locational differences in colony area are observed on day 7 and become more prominent by day 15.

Supplementary Figure 1. Ultrastructural features of tumor constructs. Representative SEM images of MCF7 cells within PF hydrogels display (A, D) a greater degree of colony formation at the edge compared to (G) the center of the hydrogel constructs and also exhibit (J) cell-cell interactions (denoted by white arrows) through (M) numerous cell-surface microvilli. SK-BR-3 cells display smaller colony formation compared to MCF7 cells which are (B, E) more numerous at the hydrogel edge compared to (H) the center regions. (K, N) Cell-cell and cell-matrix interactions are visible through surface microvilli-like features. MDA-MB-231 cells exhibit (C) elongated and invasive morphology with (F) higher cell density at the hydrogel edge compared to (I) the center of hydrogel constructs. (L, O) Elongated cells exhibit distinct cell-surface projections of varying shapes and dimensions. (M, N, O) Cell-surface projections are markedly different for the three cell types indicating heterotypic cell-matrix interactions.

Supplementary Figure 2. MCF7 colony morphology over time. Distribution of (A) colony area, (B) colony diameter, (C) colony circularity and (D) colony aspect ratio of individual MCF7 colonies in three hydrogel compositions over time (n= 50 colonies per time point per condition).

Supplementary Figure 3. SK-BR-3 colony morphology over time. Distribution of (A) colony area, (B) colony diameter, (C) colony circularity and (D) colony aspect ratio of individual SK-BR-3 colonies in three hydrogel compositions over time (n= 50 colonies per time point per condition).

Supplementary Figure 4. MDA-MB-231 cellular morphology over time. Distribution of (A) cellular area, (B) cellular diameter, (C) cellular circularity and (D) cellular aspect ratio of individual MDA-MB-231 cells in three hydrogel compositions over time. (n= 50 cells per time point per condition).

Supplementary Figure 5. MDA-MB-231 elongation length over time. MDA-MB-231cells in PF hydrogels are significantly more elongated compared to those in PF+1%P and PF+2%P hydrogels (Data presented as average of 3 independent tumor constructs, n= 50 cells per time point per condition, * significant difference between PF and PF+2%P, # significant difference between PF and PF+1%P, $p<0.05$).

Supplementary Figure 6. MDA-MB-231 elongation length over time. Distribution of cellular elongation length in three hydrogel compositions over time. (n= 50 cells per time point per condition).

Supplementary Figure 7. Locational variation in colony area. Distribution of (A) MCF7 and (B) SK-BR-3 colonies within PF-based tumor constructs reveals relatively higher increase in colony area near the hydrogel edge as compared to the interior regions over 15 days in culture. Each point represents an individual colony.

Supplementary Figure 8. Collagenase diffusion in PF-based hydrogels. Analysis of diffusion kinetics of collagenase in hydrogels of varying composition shows reduction in effective diffusion coefficients with increasing PEGDA content (n=4 hydrogels per condition, *$p<0.05$).

Supplementary Video 1. Z-stack of MCF7 cells cultured in PF hydrogels over 15 days reveals distinct spherical-shaped cell colonies located evenly throughout the entire z-section of the tumor constructs.

Supplementary Video 2. Z-stack of SK-BR-3 cells cultured in PF hydrogels over 15 days reveals distinct cell colonies throughout the entire z-section of the tumor constructs.

Supplementary Video 3. Z-stack of MDA-MB-231 cultured in PF hydrogels over 15 days reveals the invasive behavior of the cells with elongated cells with intercellular connections and protrusions appearing closer to the bottom surface of the hydrogel construct and a distinct sub-population of rounded cells appearing in the middle of construct.

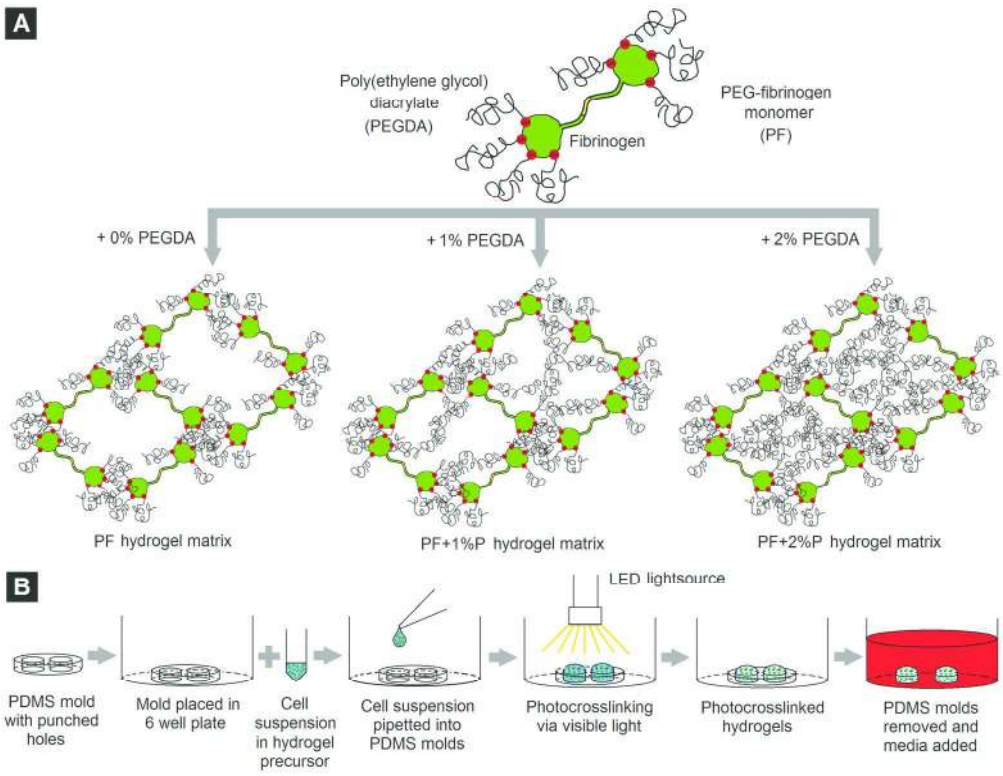

Figure 1. Schematic of hydrogel preparation and cell encapsulation. (A) PEG-fibrinogen (PF) is coupled with additional PEGDA (1% or 2% w/v) to form hydrogel matrices (PF+1%P or PF+2%P) with modified physical characteristics. (B) PDMS molds are used to form photocrosslinked cell-laden hydrogel constructs via visible light and maintained in 3D culture.

190x146mm (300 x 300 DPI)

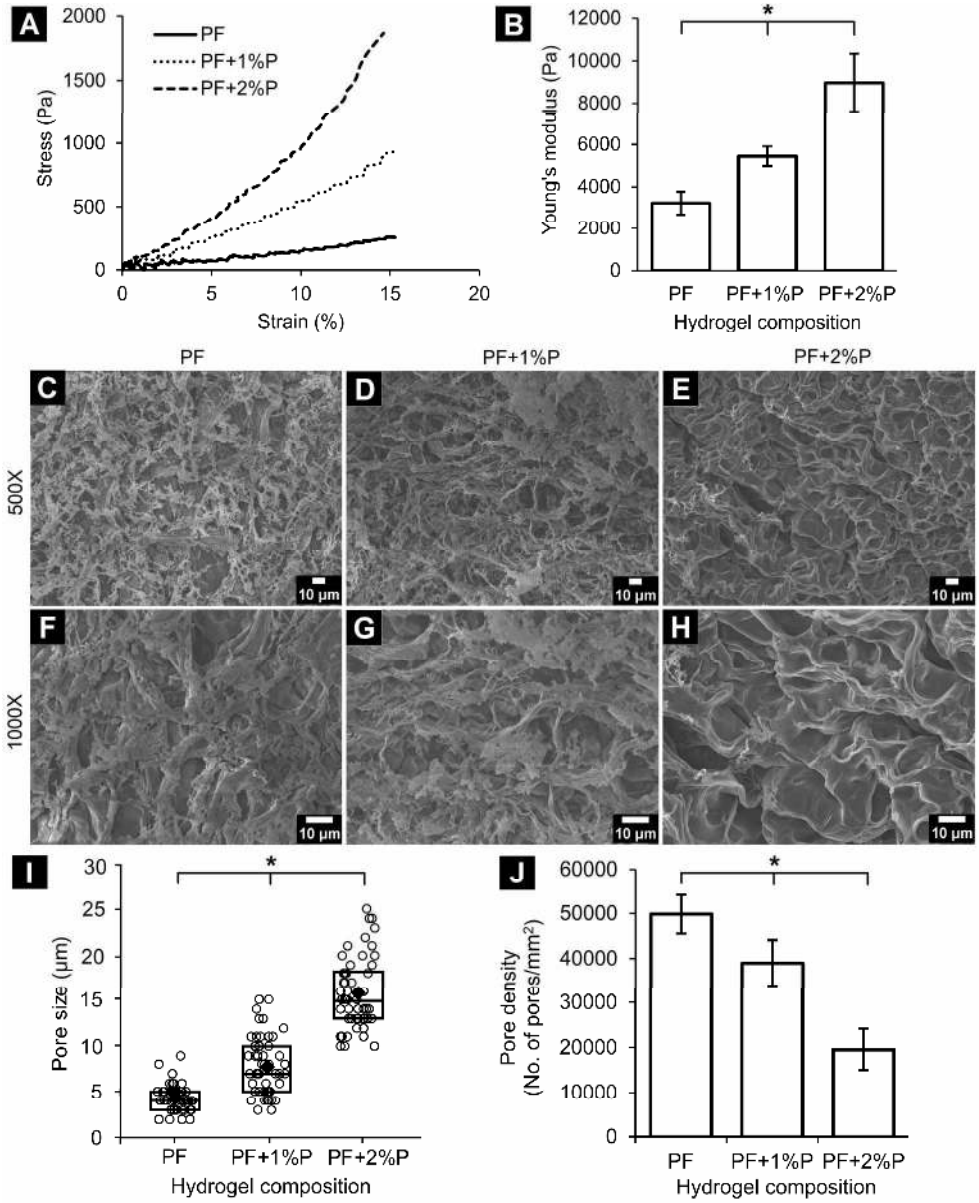

Figure 2. Mechanical and ultrastructural features of PF-based hydrogels. (A) Stress-strain relationship of PF-based tumor constructs demonstrates the influence of additional PEGDA moieties on the compressive behavior of hydrogels. (B) Incorporation of excess PEGDA results in increasing Young's modulus of tumor constructs (n=3 hydrogels, *p<0.05). (C H) Representative SEM images of acellular hydrogels of different compositions (Top panel: 500X magnification; Bottom panel: 1000X magnification). (C and F) PF hydrogels exhibit a greater degree of surface roughness due to the presence of microgrooves and sub micron pores and a higher degree of pore interconnectivity. (D and G) PF+1%P hydrogels reveal an increasing degree of groove-like features. (E and H) PF+2%P hydrogels display a smoother pore surface and a greater degree of self-supporting features. (I) Increase in pore size and (J) decrease in pore density with additional PEGDA incorporation in PF-based hydrogel matrices. Circles denote individual pore measurements, diamonds denote means of respective groups and rectangular boxes represent the lower quartile, median and upper quartile of respective groups (Pore size: n=50 pores, Pore density: n=5 representative regions of interest, *p<0.05).

190x232mm (600 x 600 DPI)

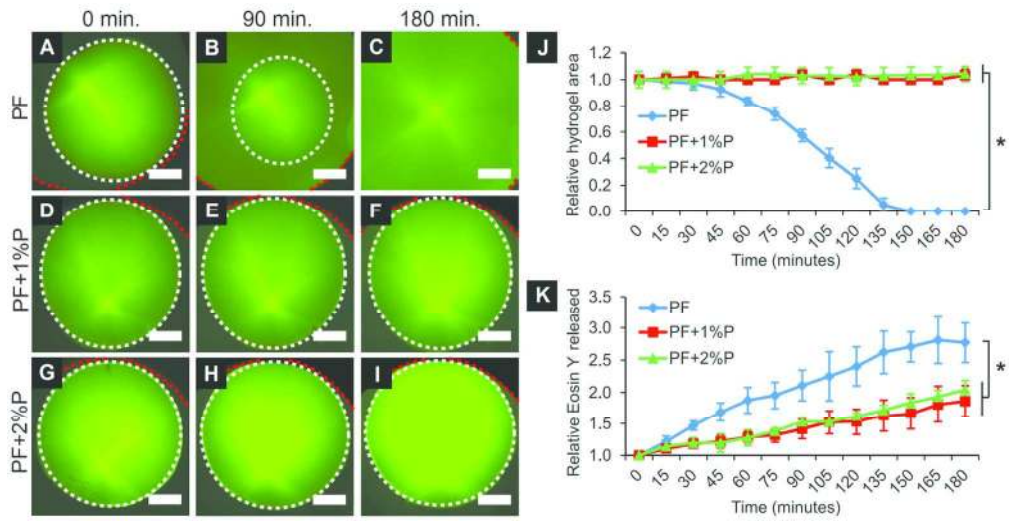

Figure 3. Degradation behavior of PF-based hydrogels. (A-C) PF hydrogels undergo complete disassembly with leaching of Eosin Y over 180 minutes. (D-E) PF+1%P hydrogels and (G-I) PF+2%P hydrogels remain intact in bulk structure over time. White line denotes the hydrogel edge and red line denotes the edge of the well. (J) PF hydrogels show significant reduction in hydrogel area compared to PF+1%P and PF+2%P hydrogels. (K) PF hydrogels undergo higher degree of Eosin Y release compared to PF+1%P and PF+2%P hydrogels (n=4 hydrogels, *p<0.05). Scale bar = 1 mm.

130x67mm (300 x 300 DPI)

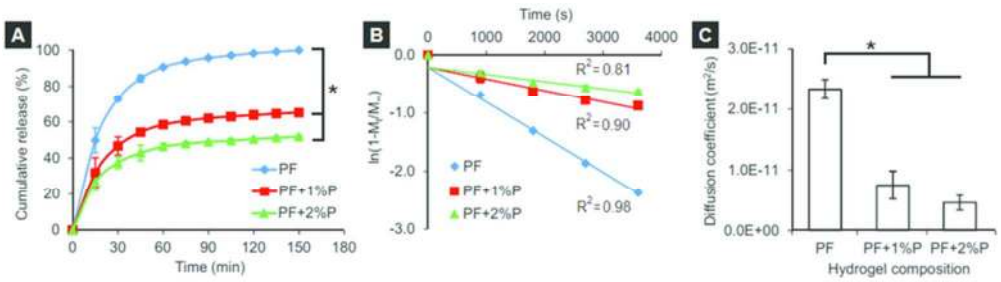

Figure 4. Release profile kinetics of PF-based hydrogels. (A) Percentage cumulative release profiles of entrapped TRITC-dextran from PF-based hydrogels demonstrate slower release rates with increasing PEGDA concentration. (B) Plot of ln(1-Mt/M∞) versus time for PF-based hydrogels. Correlation coefficients of fitted linear trendlines are presented adjacent to the respective trendlines. (C) Diffusion coefficients of TRITC-dextran released from PF-based hydrogels demonstrate significantly reduced values with the incorporation of additional PEGDA (n=4 hydrogels, *p<0.05).

70x19mm (300 x 300 DPI)

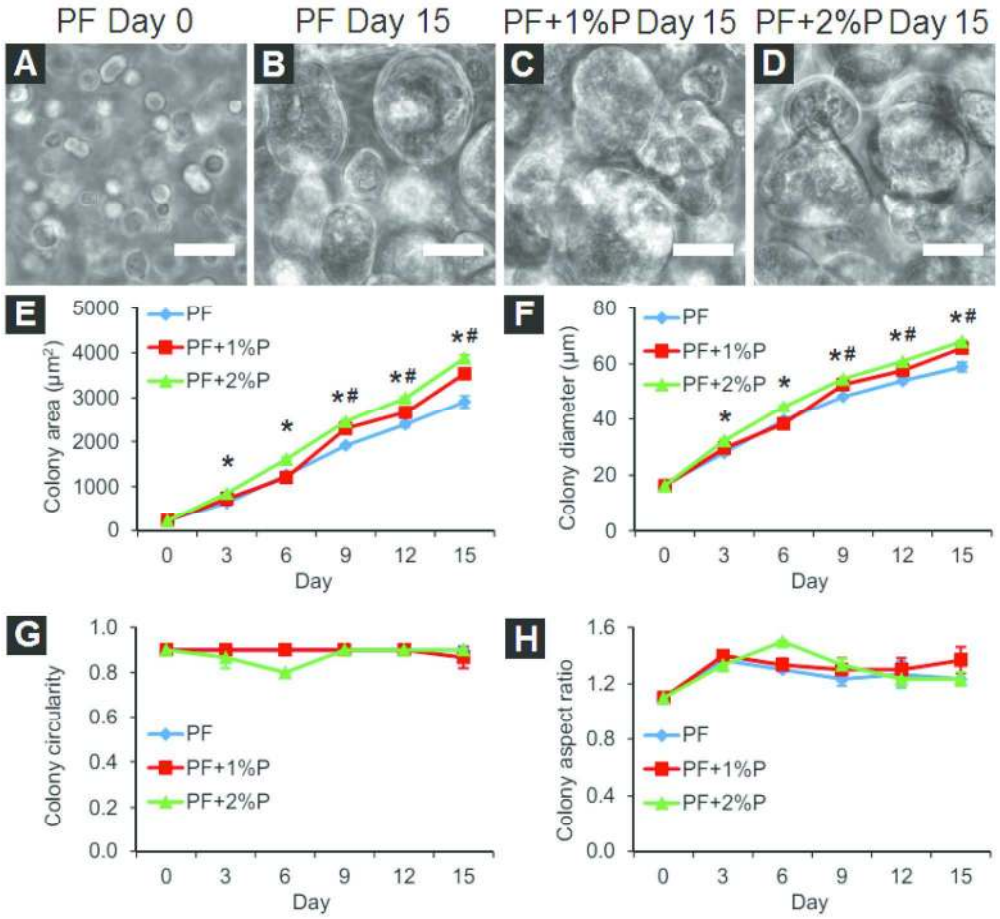

Figure 5. MCF7 colony morphology over time. (A D) Representative phase contrast images of MCF7 cells demonstrate local colony formation within PF-based hydrogels over 15 days in culture. (E) Increase in average colony area and (F) average colony diameter of MCF7 cells with time, with PF+2%P hydrogels displaying larger colony formation. (G) Average colony circularity and (H) average colony aspect ratio remain fairly constant among the three groups (Data presented as average of 3 independent tumor constructs, n = 50 colonies, * significant difference between PF and PF+2%P, # significant difference between PF and PF+1%P, $p<0.05$). Scale bar = 50 μm.

191x177mm (300 x 300 DPI)

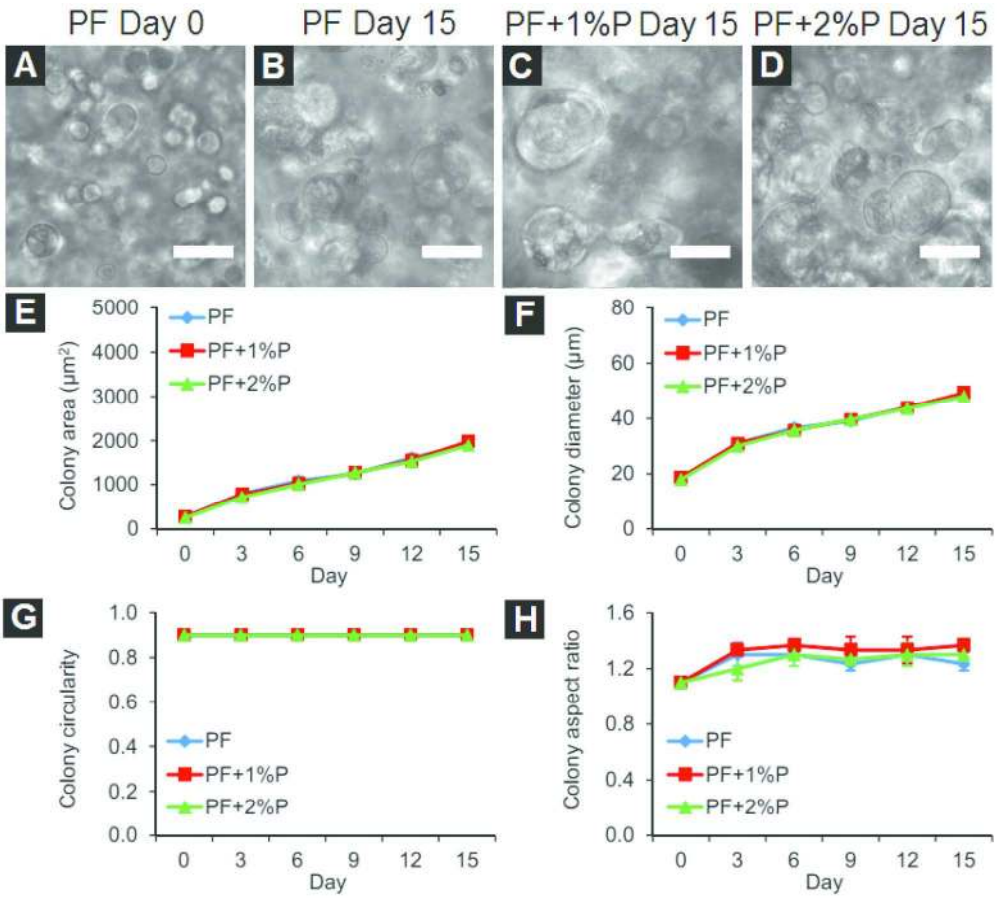

Figure 6. SK-BR-3 colony morphology over time. (A D) Representative phase contrast images of SK-BR-3 cells demonstrate local colony formation within PF-based hydrogels over 15 days in culture. (E) Increase in average colony area and (F) average colony diameter of SK-BR-3 cells with time. (G) Average colony circularity and (H) average colony aspect ratio remain fairly constant with time (Data presented as average of 3 independent tumor constructs, n = 50 colonies, no significant difference between three groups, $p<0.05$). Scale bar = 50 μm.

191x171mm (300 x 300 DPI)

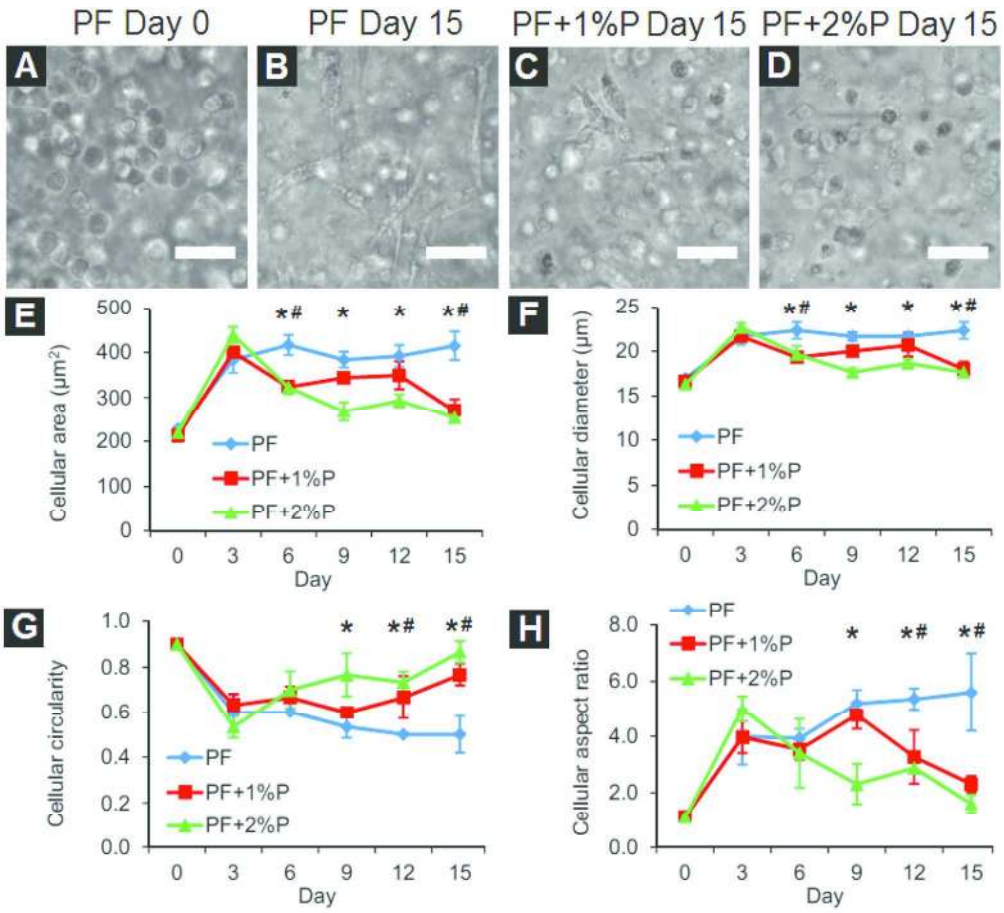

Figure 7. MDA-MB-231 cell morphology over time. (A D) Representative phase contrast images of MDA-MB-231 cells exhibit invasive and elongated morphologies within PF-based hydrogels while some cells remain spherical in shape and non committed towards an invasive morphology. (E) Cellular area and (F) cellular diameter of MDA-MB-231 cells remain fairly uniform over time, with PF hydrogels displaying higher cellular size. (G) Colony circularity and (H) colony aspect ratio are also significantly different between hydrogels of three different compositions (Data presented as average of 3 independent tumor constructs, n = 50 cells, * significant difference between PF and PF+2%P, # significant difference between PF and PF+1%P, $p<0.05$). Scale bar = 50 μm.

189x171mm (300 x 300 DPI)

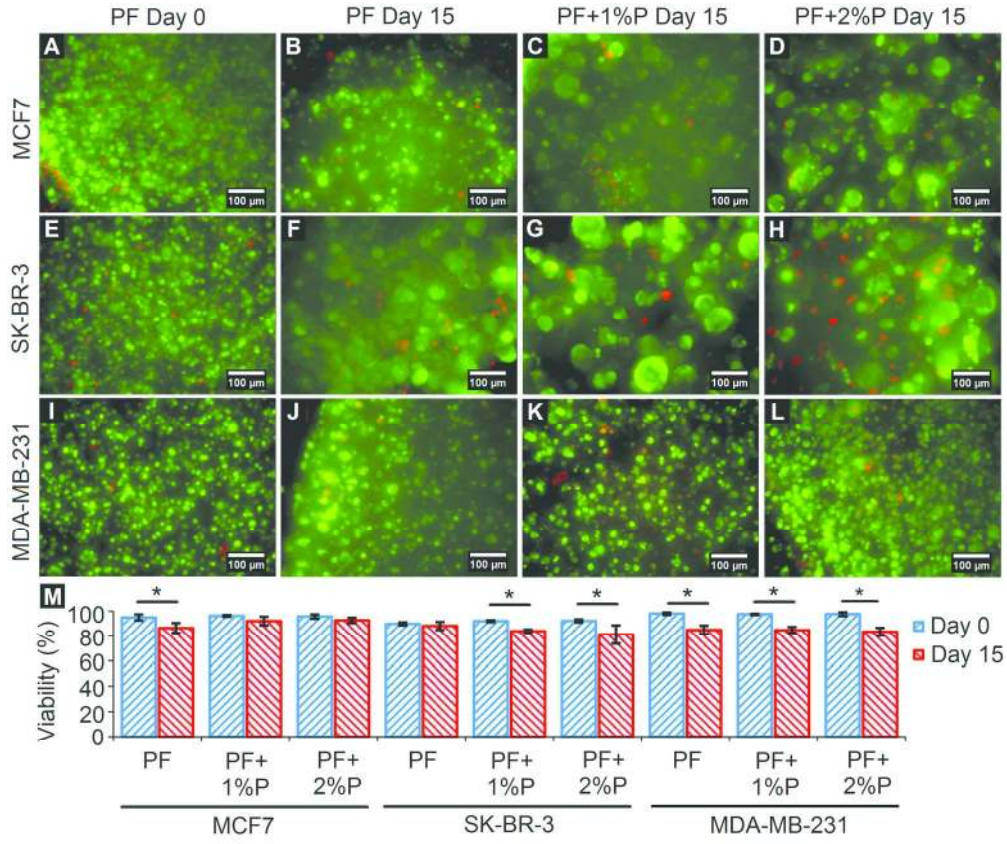

Figure 8. Cell viability in PF-based hydrogels. (A-L) Representative fluorescence z stacks (thickness = 200 µm) of cells within PF-based tumor constructs stained with calcein AM (Live, green) and ethidium homodimer (Dead, red) on days 0 and 15 demonstrate uniform distribution of live cells. (M) MCF7, SK-BR-3 and MDA MB-231 cells exhibit relatively high cell viability through 15 days of culture, irrespective of matrix stiffness, thereby demonstrating that matrix stiffness does not influence cell viability; temporal changes in viability were observed in some conditions (n = 5 z stacks from at least 3 independent tumor constructs, *p<0.05). Scale bar = 100 µm.

190x160mm (300 x 300 DPI)

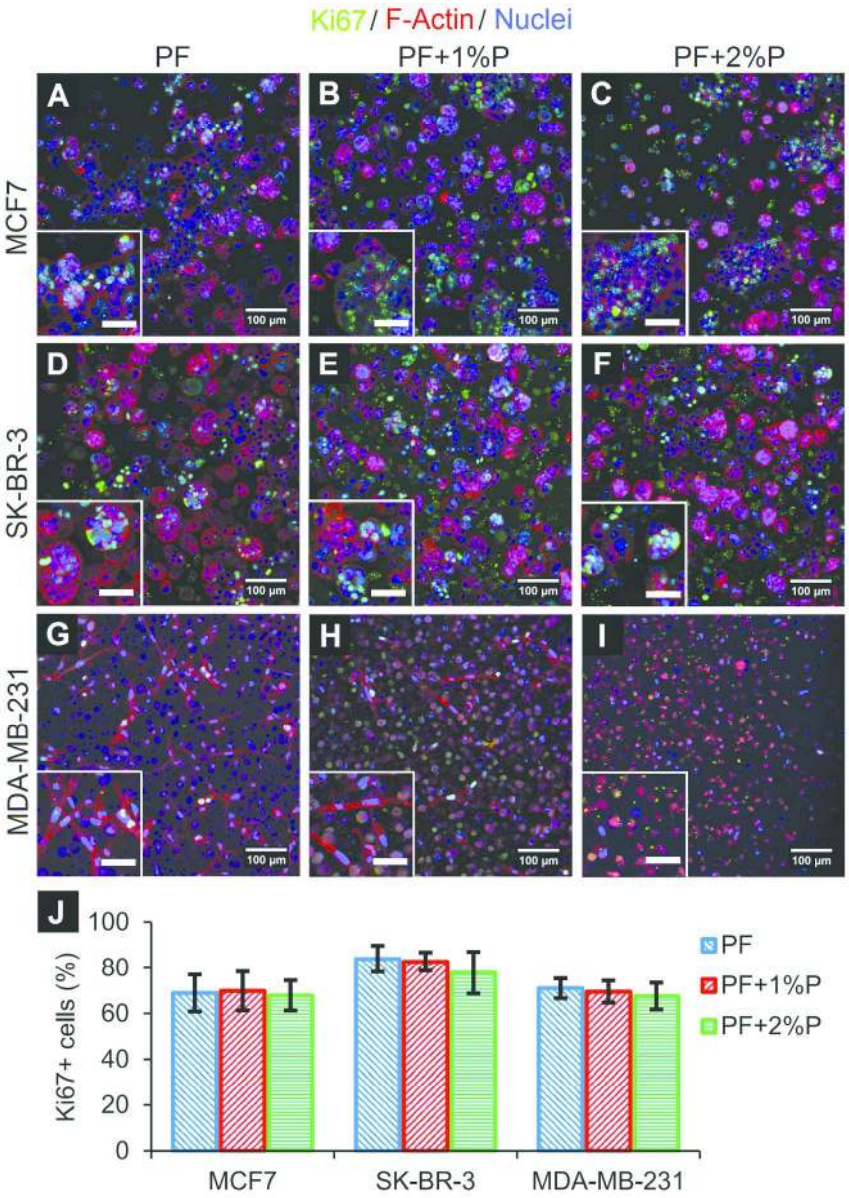

Figure 9. Cell line- and stiffness-dependent morphology and proliferation within PF-based hydrogels. (A-I) Representative fluorescence images of cells within tumor constructs on day 15 post-encapsulation. Scale bar = 100 µm. (Inset - magnified view of corresponding image, Scale bar: 50 µm). (A-C) MCF7 and (D-F) SK-BR-3 cells display local colony formation with cells stained for actin filaments (red, cell morphology), Ki67 (green, cell proliferation), and nuclei (blue). (G I) MDA-MB-231 cells display elongated morphology in PF hydrogels which decreases with increasing PEGDA content. (J) Relative percentage of Ki67 positive cells for cancer cell lines in PF based hydrogels (n= 5 z-stacks from at least 3 independent tumor constructs).

188x266mm (300 x 300 DPI)

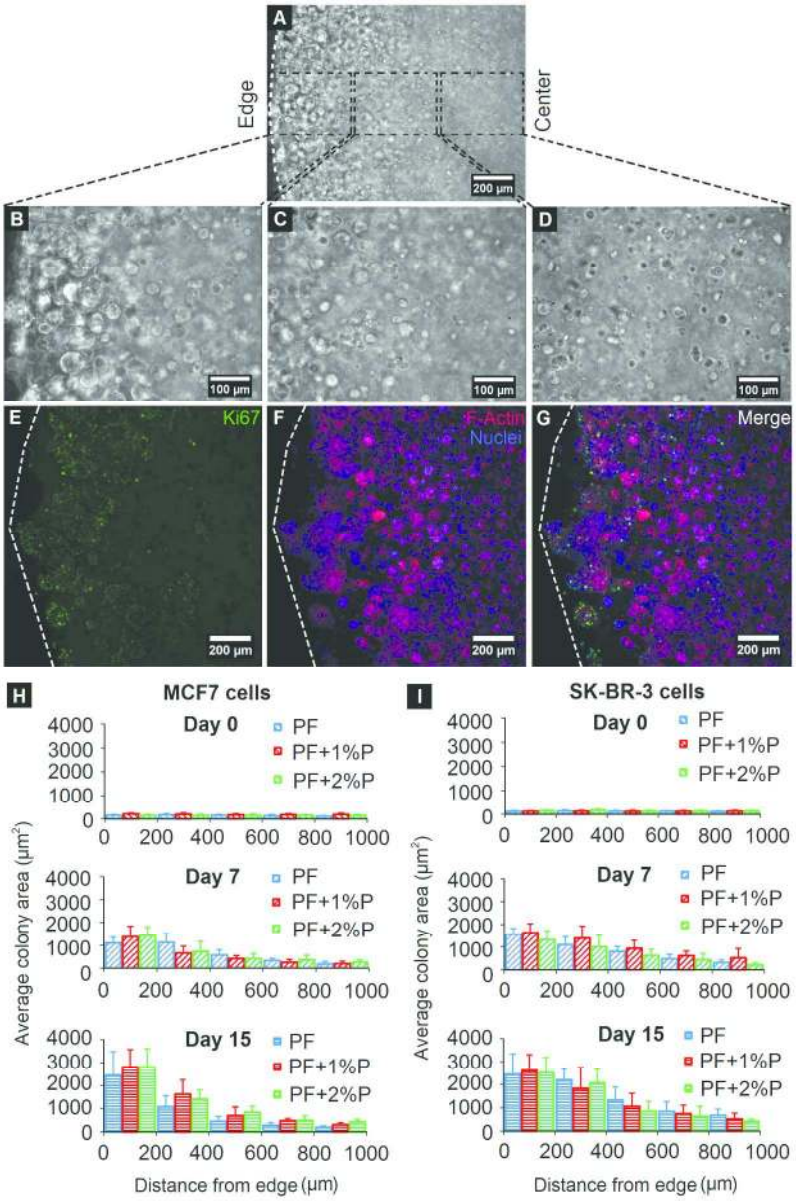

Figure 10. Locational heterogeneity in tumor constructs. Representative phase contrast images of (A) MCF7 cells cultured within PF hydrogels and imaged on day 15 exhibit locational differences in colony size with (B) those near the edge appearing largest in size, (C) those in the intermediate zone appearing smaller, and (D) those in the innermost zone appearing isolated and smallest in area. (E, F, G) Representative fluorescence images of MCF7 cells positive for Ki67 (proliferative cells) are located closer to the hydrogel edge while those in the hydrogel center appear non proliferative and quiescent. White dotted lines represent hydrogel edge. Analysis of phase contrast images of (H) MCF7 and (I) SK BR-3 cells reveal that cells are uniformly sized throughout hydrogel constructs on day 0, but locational differences in colony area are observed on day 7 and become more prominent by day 15.

189x285mm (300 x 300 DPI)